Title

Gate-tunable frequency combs in graphene-nitride microresonators

Author

Wong, Chee Wei

Publication Date

2018-03-15

Gate-tunable frequency combs in graphene-nitride microresonators

Baicheng Yao[1,2,7*,+], Shu-Wei Huang[1,8*, +], Yuan Liu[3,9,+], Abhinav Kumar Vinod[1,+], Chanyeol Choi[1], Michael Hoff[1], Yongnan Li[1], Mingbin Yu[4,10], Ziying Feng[5], Dim-Lee Kwong[4,6], Yu Huang[3], Yunjiang Rao[2], Xiangfeng Duan[5,*] and Chee Wei Wong[1,*]

[1]*Fang Lu Mesoscopic Optics and Quantum Electronics Laboratory, University of California, Los Angeles, CA, USA*

[2]*Key Laboratory of Optical Fiber Sensing and Communications (Education Ministry of China), University of Electronic Science and Technology of China, Chengdu, China*

[3]*Department of Materials Science and Engineering, University of California, Los Angeles, CA, USA*

[4]*Institute of Microelectronics, Singapore 117685, Singapore*

[5]*Department of Chemistry and Biochemistry, University of California, Los Angeles, CA 90095, USA*

[6]*Institute for Infocomm Research, Singapore, Singapore*

Present Addresses:

[7]*Cambridge Graphene Centre, University of Cambridge, Cambridge, UK*

[8]*Department of Electrical, Computer, and Energy Engineering, University of Colorado Boulder, Boulder, CO, USA*

[9]*School of Physics and Electronics, Hunan University, Changsha, China*

[10]*State Key Laboratory of Functional Materials for Informatics, Shanghai Institute of Microsystem and Information Technology, and Shanghai Industrial Technology Research Institute, Shanghai, China*

* yaobaicheng@uestc.edu.cn; shuwei.huang@colorado.edu; xduan@chem.ucla.edu; cheewei.wong@ucla.edu

[+] B. C. Yao, S. W. Huang, Y. Liu and A. K. Vinod contribute equally in this work.

Optical frequency combs are cornerstones in modern day frequency metrology, precision spectroscopy, astronomical observations, ultrafast optics, and quantum information [1,2,3,4,5,6,7]. Based on the Kerr and Raman nonlinearities in

monolithic ultrahigh-*Q* microresonators [8,9,10], chip-scale frequency combs have recently been examined, advancing studies in optical clockwork and observations of temporal cavity solitons [11,12,13,14]. The intracavity dispersion, which determines the comb formation [15,16], is however hardly amenable to electric-field tunability – whether in microcavities or fiber cavities. Arising from its exceptional Fermi-Dirac tunability and ultrafast carrier mobility [17,18,19], graphene has a complex dispersion determined by its gate-tunable optical conductivity [20,21]. It has brought about a variety of optoelectronic advances, ranging from modulators [22, 23], photodetectors [24] to controllable plasmonics [25, 26]. Here, combining the cross-disciplinary field of Dirac fermions in two-dimensional graphene, we show for the first time the gated intracavity-tunability of graphene-based optical frequency combs, by coupling the gate-tunable optical conductivity onto a photonic microresonator, thus modulating its second- and higher-order dispersions through the Fermi level. Preserving cavity quality factors up to 10^6 in the graphene-based comb, we implement a dual-layer ion-gel-gated transistor to tune the Fermi level of graphene up to 0.65 eV, under single-volt-level control. We uncover the formation of charge-tunable primary comb lines from 2.3 THz to 7.2 THz, coherent Kerr frequency combs, controllable Cherenkov radiation, and controllable soliton states – all in a single microcavity. We further demonstrate the voltage-tunable transitions from periodic soliton crystals to crystals with defects, mapped by our ultrafast second-harmonic optical autocorrelation. This heterogeneous graphene-microcavity provides a new fundamental platform for the understanding of dynamical frequency combs and ultrafast optics at the interface of single atomic layer nanoscience and ultrafast optoelectronics.

Figure 1a to 1c shows the concept and fabrication of our graphene gate-tunable Kerr frequency comb with source-drain and top gating. This is further detailed in Methods, Supplementary Sections 1 and 2. To ensure transparency and minimal effect on the resonator *Q* for coherent comb generation, we top-gate the interacting graphene to pull the Fermi level up to 0.6 eV for reduced photon absorption in the nearly-massless Dirac cone. We note that an ion-gel capacitor is implemented on top of the graphene monolayer [27] where the ionic liquid electric double layer provides a capacitance as high as ≈ 7.2

μF/cm^2 – this large value enables high doping control and comb tunability with a few-volt level gating. This is important for sharp modulation on cavity and comb dispersion, while keeping the cavity loss low. In addition to the optimized 300-nm graphene-nitride gap, we optimize the planar graphene-nitride interaction arc length to ≈ 80 μm for a large frequency comb tunability yet with minimal graphene absorption losses. Figure 1d plots the computed group velocity dispersion (β_2) and the computed third order dispersion (β_3) for tuned Fermi levels from 0.2 eV to 0.8 eV of the graphene monolayer. For each Fermi level, we note the wavelength-oscillations in both β_2 and β_3, arising from the graphene carrier relaxation oscillation lifetime captured in the resonance of the monolayer sheet conductivity. As a result, the graphene β_2 can be tuned from anomalous to normal dispersion and then back to anomalous via gate voltage, important for the nonlinear phase-matching tunability. This enables a wide and tunable frequency comb generation in the graphene based microresonator (GMR). Based on the modeled overall graphene β_2 and β_3, we model the heterogeneous microresonator for Kerr frequency comb generation. Figure 1e shows the temporal map of the comb dynamics in the GMR, via the Lugiato-Lefever equation modeling. At E_F of 0.2 eV, the Q factor is low and hence there is no comb generation. At E_F of 0.5 eV, the GMR has a $Q \approx 8 \times 10^5$, $\beta_2 \approx$ -50 fs^2/mm and $\beta_3 \approx 0$, resulting in a slow comb generation. At E_F of 0.8 eV, we observe a fast full comb generation numerically, under a Q higher than 1×10^6, $\beta_2 \approx$ -30 fs^2/mm and $\beta_3 \approx$ -400 fs^3/mm.

Figure 2a shows the electrical tuning performance of graphene in the GMR. With a fixed source-drain voltage V_{SD} of 10 mV, the source-drain current I_{SD} is tuned with the gate voltage V_G. When V_G reaches 2.4 V, I_{SD} has a minimum of 6.5 μA. Here the carrier density of the graphene monolayer reaches the Dirac point. When V_G is less than 2.4 V, graphene is *p*-doped. In a cyclic V_G tuning, a clear hysteresis loop is observed due to the electronic trapping. Correspondingly, the gate-tunable Fermi energy $|E_F|$, $|E_F| = \hbar|v_F|(\pi N)^{-1/2}$ is plotted in the bottom panel of Figure 2a [28] and noted to be ~ $(V_G)^{1/2}$. In our experiment, we tune V_G in range of -2 V to 0 V, thereby controlling the graphene $|E_F|$ between 0.65 eV to 0.45 eV. For V_G = 0 V, the graphene monolayer in our GMR is already heavily doped, which is significant for the dispersion tuning with a low loss.

Figure 2b maps the calculated real and imaginary parts of the GMR, varying with $|E_F|$ and wavelength λ. In the two maps, the blue curves denote the boundary where dispersion dramatically changes, and the yellow curve denotes the low loss region. In our measurement, we apply a high-power CW pump at 1600 nm. At this wavelength, when we tune the $|E_F|$ from 0.45 eV to 0.65 eV, n_{eff} is controlled from $1.789 + 0.058i$ to $1.781 + 0.001i$. Figure 2c shows the measured transmissions and wavelength-FSR dependences of the GMR, under different gate voltages. In this measurement, a broadband tunable laser serves as the light source with less than 10 mW, below comb generation threshold. For a selected resonance around 1600 nm, when V_G tuned from 0 V to -2 V, the extinction ratio increases from 63% to 84%, with resonance linewidth *decreases* from 3.1 pm to 1.6 pm. Across the whole spectrum, the mode non-equidistance D_{FSR} refers the group velocity dispersion (GVD) as $D_{FSR} = -\beta_2 c(2\pi f_{FSR})^2/n_{eff}$, here c is the light velocity in vacuum [13]. It is 320 kHz/mode under $V_G \approx -1$ V (anomalous dispersion), while -45 kHz/mode under $V_G \approx -1.8$ V (normal dispersion). More details are shown in Extended Data Figure 1.

Figure 2d shows the gate tuning performance of the GMR. When the gate voltage is between 0 V to -2 V, the Fermi level remains higher than 0.4 eV and thus graphene linear absorption in our working spectral range around 1600 nm is dramatically inhibited due to the Pauli blocking. As a result, the loaded Q factor of the GMR increases from $\approx 6 \times 10^5$ to 10^6, enabling comb generation under a 1 W pump, which is critical for both protecting the graphene monolayer from damage and stabilizing the frequency combs. We also note that the Q factor deterioration is induced by both the etching process and the linear absorption of the graphene heterostructure (Extended Data Figure 2). For applications that requires higher Q factor, other two-dimensional materials such as transition metal dichalcogenides with intrinsic bandgaps, e.g. WSe_2, can also be applied to construct the heterogeneous microcavities [29]. Simultaneously, the dispersion of the resonator is dynamically tuned, varying continuously from -62 fs^2/mm anomalous dispersion to +9 fs^2/mm normal dispersion. The GVD tuning mainly results from the graphene's Dirac-Fermi dynamics [30], with smaller contributions from the ion transport and thermal effects in the ion-gel.

Next we pump the GMR with a 2 W continuous-wave laser power, with the primary comb lines (strongest frequency combs generated from modulation instability initiation) shown in Figure 3a under different gate voltages. For applied V_G = -1 V, -1.2 V, and -1.5 V, the measured frequency offset between the primary comb line and the pump Δf_{pri}, proportional to $(1/\beta_2)^{1/2}$, is observed at 2.36 THz, 3.25 THz, and 7.17 THz respectively. When V_G = -1.8 V, GVD of the GMR becomes positive and hence is harder for phase-matching without local mode-crossing-induced dispersion. Figure 3b shows the optical spectra, under carefully controlled laser-cavity detuning. Particularly, at V_G = -1 V, GVD $\beta_2 \approx$ -62 fs^2/mm while TOD $\beta_3 \approx$ -9 fs^3/mm, the Kerr comb has a span of ≈ 350 nm, with highly symmetrical shape. Interestingly, with V_G = -1.2 V, $\beta_2 \approx$ -33 fs^2/mm while $\beta_3 \approx$ -630 fs^3/mm, we observe a frequency comb spectra spanning over 600 nm, consistent with the general route of a smaller GVD bringing about a broader comb spectrum. The comb spectrum is highly asymmetric, with the red-side comb line intensity contributions from Cherenkov radiation. The spectral peak of the Cherenkov radiation is determined by $3\beta_2/\beta_3$, matching with the measurement results. In addition, such soliton perturbation and energy transfer can be utilized to stabilize the Kerr frequency comb [13]. Thirdly, when V_G = -1.5 V, $\beta_2 \approx$ -8 fs^2/mm while $\beta_3 \approx$ -213 fs^3/mm. Since β_2 here is quite small (less than 10 fs^2/mm), it does not support a stable Kerr comb, the observed comb lines are not even, and the Cherenkov peak in the spectral is also indistinguishable.

Figure 3c summarizes the gate tunability of the graphene Kerr combs, with V_G from 0 V to -2 V. For primary comb lines, their relative spectral location $\Delta f_{pri} = |f_{pri}-f_{pump}|$ is dramatically controlled, from 2.3 THz to 7.2 THz with V_G only from -1.0 V to -1.5 V respectively. This modulation matches the GVD engineering well, as well as influenced by the slight nonlinearity enhancement brought by the graphene. For full-generated combs, we also demonstrate the electric-field control on their spectral span, across 38 THz to 82 THz with V_G from -1.0 V to -1.3 V (for this device, $|V_G|$ more than 1.3 V does not show a good coherent comb state). Moreover, we also note the gate-tuning changes the FSRs of the combs, from 89.6 GHz at -1.0 V to 89.9 GHz at -1.5 V. Such an optoelectronic tunability enables different Kerr frequency combs with a variety of properties existing in the same device. Figure 3d next illustrates the measured locations of the Cherenkov peaks, in comparison with the computed designs. In contrast to the primary comb lines, the TOD plays an important role in the Cherenkov radiation. We observed three Cherenkov peaks in the 1400 nm the 2000 nm window, with spectral locations $\Delta f_c = |f_c\text{-}f_{pump}|$ spanning from 26.3 THz (V_G = -1.2 V), 49.2 THz (V_G = -1.3 V), and 17.7 THz (V_G = -1.5 V). They satisfy the calculated results well. We note that, in Figure 3c and 3d, results are collected in the region of -0.4 V to -1.6 V since, when V_G is more than -0.4 V, the Q factor of the GMR is too low for comb generation and, when V_G is less than -1.6 V, the GVD is too small to ensure a stable comb.

We estimate the modulation speed of the GMR in Figure 3e. With V_G tuning, the output comb line intensity within the filter window is modulated temporally. The modulation speed here is bounded by ion diffusion in the heterostructure, large ion-gel capacitance on the graphene, and the optical filter bandwidth. In our current proof-of-principle demonstration, we use the ion-gel based capacitor to ensure $|E_F|$ is sufficiently high, whose large capacitance (7.2 μF/cm^2) and slow ion diffusion ($\approx 10^{-10}$ m^2/s) limits the charge-discharge operation speed to less than hundreds of kHz. Optical filter bandwidth can be narrowed to improve the detection rate of the modulation by almost 7.5× in Figure 3e, we show the modulated signal-to-noise ratio (SNR) with a RF spectrum analyzer, by using optical filters with passband width of 50 nm, 9 nm, and 2 nm respectively Their corresponding bandwidths are 80 kHz, 200 kHz and 600 kHz. (Extended Data Figure 3). Here, although sub-MHz modulation for the primary comb is successfully demonstrated, we have to note that fast modulation while preserving the full-grown Kerr comb across the entire modulation cycle could be much more challenging: with V_G tuning, not only the GVD, but also the FSR of the GMR is tuned. Compared to the primary combs shown in Figure 3a, phase-matching of the full combs in Figre 3b is much more sensitive, a slight variation in the FSR from the gate modulation may cause the Kerr comb to collapse. To achieve reliable fast on-off switching in full-generated Kerr combs, inverse FSR compensation (e.g. via temperature feedback) should be applied. Such a sub-MHz tunability for a Kerr comb could be potential in diverse applications [31] such as tunable THz applications and precision measurements.

Dispersion is one of the most critical cavity parameter that defines the Kerr frequency comb dynamics. The significant broadband dispersion modulation, controlled by the gate voltage of the graphene-nitride heterogeneous microresonator, opens up the possibility of dynamically selecting the formation path of dissipative Kerr solitons and frequency combs. By using the gate tunable GMRs, we can engineer the dispersion dynamically for diverse soliton states formation via electrical control. With a fixed pump power of 2 W, Figure 3f counts our achieved soliton states in the measurements with the same experimental condition, when the gate voltage in range of -1.6 V to -1.1 V. In total, we have found soliton states with soliton number of 12, 11, 9, 8, 6, 5 and 4. More theoretical calculations and simulations are discussed in Supplementary section S1.4.

Figure 4 demonstrates four specific examples of the soliton crystal states, under optimized gate voltages. Here the left panels show the measured intensity transmission, the middle panels demonstrate the optical spectra, and the right panels illustrates the frame-by-frame frequency-resolved second-harmonic autocorrelation maps. These soliton states with low RF noise are achieved following Turing patterns and chaotic states before transition into the soliton states (Extended Data Figure 4). This is characterized by transmission step, by tuning the pump laser gradually into the cavity resonance. Figure 4a shows two examples of the soliton state with missing pulses, at a gate voltage V_G of -1.2 V. The corresponding pump laser wavelength is around 1600.2 nm. The optical spectra of these states are characterized by the apparent existence of groups of comb lines that are separated by multiple cavity FSRs. Within each comb group, weaker single-FSR comb lines are present and they effectively connect all comb groups without any spectral gaps. For the examples shown on Figure 4a and 4d, the comb groups are separated by 8 FSR, 5 FSR and 12 FSR respectively. In the time domain, the AC traces reveal the common features of missing pulses in the otherwise equally spaced soliton states with higher effective repetition rate. The self-organization of multiple soliton pulses into equally spaced soliton pulse train resembles the crystallization process, or termed a soliton crystal [32], and the missing pulse structure is analogous to defects in crystal lattices. Our graphene-nitride heterogeneous microresonator thus provides a platform for gate-voltage and Femi-level tunable study of the soliton physics. We also note that, when the soliton crystals are formed, the emitted soliton Cherenkov radiations are sharp and narrow, marked by the grey arrows.

Soliton crystals are formed due to the strong mode interaction and intra-cavity interferences, and thus their evolution dynamics depend critically on the exact dispersion profile of the microresonator. By further optimizing the GVD and TOD via gate tuning, we demonstrate two periodic soliton crystal states. Figure 4b shows a 4-soliton state with

V_G = -1.3 V and pump laser at ≈ 1584.2 nm, while Figure 4c shows a 11-soliton state with V_G = -1.4 V and pump laser at ≈ 1600.1 nm. Intriguingly these soliton crystal states show remarkable stability and they can robustly survive a significant pump power fluctuation up to ± 2 dB, or wavelength offset up to ± 300 pm. The soliton crystal formation is also akin to harmonic mode-locking where stable high-repetition-rate pulse train can be attained even in longer cavities, and it attracts interests in applications such as high-speed communication, comb spectroscopy, and data storage. This first realization of the charge-tunable graphene heterostructure for controllable frequency combs and soliton dynamics opens a new architecture at the interface of single atomic layer nanoscience and ultrafast optoelectronics.

References

1. Udem, T., Holzwarth, R. & Hansch, T. Optical frequency metrology. Nature **416**, 233–237 (2002).
2. Kippenberg, T., Holzwarth, R. & Diddams, S. Microresonator-based optical frequency combs. Science **332**, 555–559 (2011).
3. Cingoz, A., Yost, D., Allison, T., Ruehl, A. & Fermann, M., Hartl, I. & Ye, J. Direct frequency comb spectroscopy in the extreme ultraviolet. Nature **482**, 68–71 (2012).
4. Ideguchi, T., Holzner, S., Bernhardt, B., Guelachvili, G., Picqué, N. & Hansch, T. W. Coherent Raman spectro-imaging using laser frequency combs. Nature **502**, 355–358 (2013).
5. Steinmetz, T., Wilken, T., Araujo-Hauck, C., Holzwarth, R., Hansch, T., Pasquini, L., Manescau, A., D'Odorico, S., Murphy, M., Kentischer, T., Schmidt, W. & Udem, T. Laser frequency combs for astronomical observations. Science **321**, 1335–1337 (2008).
6. Huang, S.-W., Zhou, H., Yang, J., McMillan, J. & Matsko, A., Yu, M., Kwong, Maleki, L. & Wong, C. W. Mode-locked ultrashort pulse generation from on-chip normal dispersion microresonators. Phys. Rev. Lett. **114**, 053901 (2015).
7. Saglamyurek, E., Sinclair, N., Jin, J., Slater, J., Oblak, D., Bussières, F., George, M., Ricken, R., Sohler, W. & Tittel, W. Broadband waveguide quantum memory for entangled photons. Nature **469**, 512–515 (2011).

---

8. Del Haye, P., Schliesser, A., Arcizet, O., Wilken, T., Holzwarth, R. & Kippenberg, T. Optical frequency comb generation from a monolithic microresonator. Nature **450**, 1214–1217 (2007).
9. Moss, D. J., Morandotti, R., Gaeta, A. L., & Lipson, M. New CMOS-compatible platforms based on silicon nitride and Hydex for nonlinear optics. Nature Photon. **7**, 597–607 (2013).
10. Yang, Q. F., Yi, X., Yang, K. Y., & Vahala, K. Stokes solitons in optical microcavities. Nature Phys. **13**, 53–58 (2016).
11. Xue, X., Xuan, Y., Liu, Y., Wang, P. & Chen, S. Wang, J., Leaird, D., Qi, M. & Weiner, A. Mode-locked dark pulse Kerr combs in normal-dispersion microresonators. Nature Photon. **9**, 594–600 (2015).
12. Huang, S.-W., Yang, J., Yu, M., McGuyer, B. & Kwong, D. Zelevinsky, T. & Wong, C. W. A broadband chip-scale optical frequency synthesizer at 2.7×10^{-16} relative uncertainty. Science Adv. **2**, 1501489 (2016).
13. Brasch, V., Geiselmann, M., Herr, T., Lihachev, G. Pfeiffer, M., Gorodetsky, M., & Kippenberg, T. Photonic chip–based optical frequency comb using soliton Cherenkov radiation. Science **351**, 357–360 (2016).
14. Marin-Palomo, P., Kemal, J. N., Karpov, M., Kordts, A., Pfeifle, J., Pfeiffer, M. H. P, Trocha, P., Wolf, S., Brasch, V., Anderson, M. H., Rosenberger, R., Vijayan, K., Freude, W., Kippenberg, T. J., & Koos, C. Microresonator-based solitons for massively parallel coherent optical communications. Nature **546,** 274–279 (2017).
15. Del Haye, P., Coillet, A., Fortier, T., Beha, K., Cole, D., Yang, K., Lee, H., Vahala, K., Papp, S. & Diddams, S. Phase-coherent microwave-to-optical link with a self-referenced microcomb. Nature Photon. **10**, 516–520 (2016).
16. Herr, T., Brasch, V., Jost, J. Wang, C. & Kondratiev, N. Temporal solitons in optical microresonators. Nature Photon. **8**, 145–152 (2014).
17. Wang, F., Zhang, Y., Tian, C. Girit, G. & Zettl, A. Crommie, M. & Shen, Y. Gate-variable optical transitions in graphene. Science **320**, 206–209 (2008).
18. Li, Z., Henriksen, E., Jiang, Z., Hao, Z. & Martin, M. Dirac charge dynamics in graphene by infrared spectroscopy. Nature Phys. **4**, 532–535 (2008).

---

19. Bonaccorso, F., Sun, Z., Hasan, T. & Ferrari, A. Graphene photonics and optoelectronics. Nature Photon. **4**, 611–622 (2010).

20. Vakil, A. & Engheta, N. Transformation optics using graphene. Science **332**, 1291–1294 (2011).

21. Gu, T., Petrone, N., McMillan, J., Zande, A., Yu, M., Lo, G. Kwong, D., Hone, J. & Wong, C. W. Regenerative oscillation and four-wave mixing in graphene optoelectronics. Nature Photon. **6**, 554–559 (2012).

22. Liu, M., Yin, X., Avila, E., Geng, B., Zentgraf, T., Ju. L., Wang, F. & Zhang, X. A graphene-based broadband optical modulator. Nature **474**, 64–67 (2011).

23. Phare, C., Lee, Y., Cardenas, J. & Lipson, M. Graphene electro-optic modulator with 30 GHz bandwidth. Nature Photon. **9**, 511–514 (2015).

24. Koppens, F., Mueller, T., Avouris, P., Ferrari, A., Vitiello, M. & Polini, M. Photodetectors based on graphene, other two-dimensional materials and hybrid systems. Nature Nanotech. **9**, 780–793 (2014).

25. Grigorenko, A., Polini, M., & Novoselov, K. Graphene plasmonics. Nature Photon. **6**, 749–758 (2012).

26. Chakraborty, S., Marshall, O., Folland, T., Kim, Y., Grigorenko, A. & Novoselov, K. Gain modulation by graphene plasmons in aperiodic lattice lasers. Science **351**, 246–248 (2015).

27. Xu, Y., Lin, Z., Zhong, X., Huang, X., Weiss, N., Huang, Y. & Duan, X. Holey graphene frameworks for highly efficient capacitive energy storage. Nature Comm. **5**, 4554 (2014).

28. Das, A., Pisana, S., Chakraborty, B., Piscanec, B., Saha, S., Waghmare, U., Novoselov, K., Krishnamurthy, H., Geim, A., Ferrari, A. & Sood, A. Monitoring dopants by Raman scattering in an electrochemically top-gated graphene transistor. Nature Nanotech. **3**, 210–215 (2008).

29. Javerzac-Galy, C., Kumar, A., Schilling, R., Piro, N., Khorasani, S., Barbone, M., Goykhman, I., Khurgin, J., Ferrari, A. & Kippenberg, T. Excitonic emission of monolayer semiconductors near-field coupled to high-Q microresonators. arXiv:1710.04294 (2017).

---

30. Sorianello, V., Midrio, M., Contestabile, G., Asselberg, I., Van Campenhout, J., Huyghebaerts, C., Goykhman, I., Ott, A. K., Ferrari, A. C. & Romagnoli, M. Graphene phase modulator. Nature Photon. **12,** 40–44 (2018).

31. Huang, S., Yang, J., Yang, S., Yu, M., Kwong, D., Zelevinsky, T., Jarrahi, M. & Wong, C. Globally stable microresonator Turing pattern formation for coherent high-power THz radiation on-chip. Phys. Rev. X **7,** 041002 (2017).

32. Cole, D., Lamb, E., DelHaye, P., Diddams, & S., Papp, S. Soliton crystals in Kerr resonators. Nature Photonics **11**, 671-675 (2017).

Supplementary Information. Supplementary information is available in the online version of the paper. Reprints and permissions information is available online at www.nature.com/reprints.

Acknowledgements. The authors thank Jinghui Yang, Bowen Li, Tatsuo Itoh, Hao Liu, and Xu Xie for discussions. Graphene fabrication was supported by the Nanoelectronics Research Facilities (NRF) of UCLA. The authors acknowledge support from the National Science Foundation (DMR-1611598, CBET-1520949 and EFRI-1741707), the University of California – National Laboratory research program (LFRP-17-477237), the Office of Naval Research (N00014-16-1-2094), and the Air Force Office of Scientific Research (FA9550-15-1-0081). X.F.D. acknowledges support from the Office of Naval Research (N00014-15-1-2368) and Y.H. acknowledges support from the National Science Foundation (EFRI-1433541). This work is also supported by the National Science Foundation of China (61705032) and the 111 project of China (B14039).

Author contributions. B.C.Y., S.-W.H., Y.L. and A.K.V. contributed equally in this study. B.C.Y. and S.-W.H. designed and led the work on the graphene-nitride frequency combs including the first and detailed measurements, the gated-tuned ultrafast optics measurements, and the numerical designs. Y.L. and Z.Y.F. designed, performed graphene-nitride integration, conducted relevant electrical measurements and device optimizations. B.C.Y., C.C., S.-W.H., M.H., M.Y. and D.-L.K. performed silicon nitride chip and device processing. Y.H. and X.F.D. supervised graphene material preparation, device fabrication and electronic measurements. B.C.Y., A.K.V., S.-W.H. and C.W.W. performed the measured data analysis, on the frequency comb, RF and ultrafast correlation measurements. S.-W.H., B.C.Y., and Y.N.L. provided the theory and numerical calculations. All authors discussed the results. B.C.Y., S.-W.H., Y.L., Y.J.R. and C.W.W. prepared the manuscript. C.W.W. led and supported this research.

Author Information. Reprints and permissions information is available at www.nature.com/reprints. The authors declare no competing financial interests. Readers are welcome to comment on the online version of the paper. Correspondence and requests for materials should be addressed to B.C.Y., S.W.H., X.F.D., and C.W.W. (yaobaicheng@uestc.edu.cn; shuwei.huang@colorado.edu; xduan@chem.ucla.edu; cheewei.wong@ucla.edu).

Figure 1 | Conceptual design and implementation of the gate-tunable graphene-nitride heterogeneous microcavity. a, Schematic architecture of the GMR. A graphene/ion-gel heterostructure is incorporated in the nitride microresonator. **b,** *E*-field distribution of the graphene-nitride heterogeneous waveguide, with a Si_3N_4 cross section of $1.2 \times 0.8\ \mu m^2$. The distance between the Si_3N_4 waveguide and the graphene layer is 100 nm. Graphene and the top gate probe is separated by 1 μm with the interlayer ion-gel capacitor. In this structure, TE mode is applied. **c,** Optical micrographs show the bus waveguide (red arrows), ring resonator and Au/Ti metallized patterns. An etched window is designed to ensure both the graphene-light interaction and a reduced propagation loss. Here the graphene covered area is marked by the grey dashed box. Scale bar: 100 μm. **d,** Calculated group-velocity-dispersion (GVD) and third-order-dispersion (TOD) of graphene, depending on its Fermi-level. Here the curves with $|E_F| = 0.5$ eV and $|E_F| = 0.6$ eV, corresponding to the experimental conditions, are highlighted in yellow and red respectively. **e,** Simulated Kerr comb dynamics in the GMR, with different dispersion curves determined by the graphene Fermi level.

Figure 2 | Gate-tuning the graphene microring resonator. a, Electronic measurement of the graphene / ion-gel capacitor. At a source-drain voltage V_{SD} of 10 mV, the 'V_G - I_{SD}' correlation shows the Dirac point position and tunable Fermi level of the graphene layer. **b,** Theoretically modeled GMR complex refractive index as a function of Fermi levels and optical wavelengths, where the dispersion and the *Q* can be deduced from the real and imaginary components. Measured data points are shown in white, at a wavelength 1600 nm, with $|E_F|$ from 0.5 eV to 0.7 eV. **c,** Measured transmissions (top panel) and mode FSR (bottom panel, dots: measured, curves: linear fitting) of the GMR, under gate voltages V_G from 0 V to -2 V. **d,** Tuned *Q* factor and dispersion, under various V_G. The *Q* factor increases from 6×10^5 to 1×10^6 while the GVD is controlled between -62 fs^2/mm to +9 fs^2/mm. Error bar is the measurement uncertainty estimated from FSR measurements under the same condition.

Figure 3 | Observations of the gate-tunable graphene Kerr frequency combs. a, Primary comb lines at controlled gate voltages and Fermi levels of graphene. **b,** Full frequency combs generated under gate voltages of -1 V, -1.2 V, -1.5 V, and -1.8 V. Here the launched pump power is fixed at 34.5 dBm. Kerr combs are generated via fine-adjustment of the pump wavelength. Peaks of the Cherenkov radiation are marked by the grey arrows. **c,** Gate voltage tunes not only the primary comb line locations (blue circles) but also the full comb bandwidth (red diamonds). **d,** Frequency spacing between the CW pump and the Cherenkov radiation, which is proportional to β_2/β_3. **e,** 3-dB modulation bandwidths of 80 kHz, 200 kHz and 600 kHz are demonstrated by using optical filters with passband bandwidths of 50 nm, 9 nm and 2 nm respectively. The modulation speed is currently bounded by the ion-gel capacitance. **f,** Statistical distribution of the measured soliton states, with the same experimental parameters except for V_G tuned from -1.1 V to -1.6 V.

Figure 4 | Soliton crystals of the gated graphene-nitride microresonator. a and **d,** Soliton state with crystal-like defects including the single-soliton defect in panel **a**. Panels **c** and **d,** Periodic soliton crystal states with equally spaced soliton pulses. Panels **a** to **d** are achieved with gate voltage V_G tuned from -1.2 V to -1.5 V respectively. Left panels: measured intensity transmission, illustrating the characteristic steps associated with soliton formation. Middle panels: corresponding optical spectra measurements. The pump locations are marked by black dashed line and the Cherenkov radiation peaks are marked by grey arrows. Right panels: frequency-resolved second-harmonic autocorrelation maps of the soliton pulses. Here the grey curves show the real-time autocorrelation intensity traces.

Methods

Theoretical analysis. Refractive index of the graphene n_G is determined by graphene permittivity $\varepsilon_G = \{- Im(\sigma_G)+ iRe(\sigma_G)\}/\{2\pi f\Delta\}$ [20], where σ_G is the graphene conductivity, f is the optical frequency, and Δ = 0.4 nm is the thickness of the monolayer graphene. Particularly, $\partial^n Re(n_G) / \partial\lambda^n$ refers the nth order dispersion, while the $Im(n_G)$ refers the waveguide loss. Here the permittivity of the graphene monolayer is determined by its conductivity. In Supplementary section S1.1, we summarize the transmission and effective permittivity of graphene is determined by its quasi Fermi level E_F. By gating graphene via external field, one can control both the group velocity dispersion β_2 and the third order dispersion β_3 of a graphene monolayer conveniently. Kerr comb generation in time domain is governed by the well-known Lugiato-Lefever equation (LLE) in the GMR. In Supplementary Section S1.2, we analyze the comb formation dynamics by LLE modeling. In Supplementary Section S1.3, we describe the third-order nonlinearity of graphene. In Supplementary Section S1.4, we provide the detailed simulations about the soliton generations in the GMR.

Device design and fabrication. First, a high-Q silicon nitride microresonator is nanofabricated in a silicon foundry with measured loaded $Q \approx 1.6 \times 10^6$ (intrinsic Q of $\approx 1.8 \times 10^6$) and free-spectral range (FSR) of ≈ 90 GHz in a 350 μm diameter ring structure. The nitride core has a 1200×800 nm^2 cross-section, a 600 nm gap to the input-output coupling waveguide of 1000×800 nm^2 cross-section, and a top oxide cladding. Next the single atomic layer graphene is grown via chemical vapor deposition and transferred onto the exposed region of the nitride ring (with etched SiO_2 window). The monolayer graphene is lithographically cut into a 80×100 μm^2 sheet. Next we deposited and patterned the source-drain electrodes (Ti/Au, 20/50 nm) using electron-beam evaporation and electron-beam lithography. Here the pad size was 80 μm × 60 μm. Subsequently, we integrated ionic liquid [DEME-TFSI] as the gate dielectric, resulting an electric dual-layer graphene transistor. More details are shown in Supplementary Section 2 and Supplementary Figure S12.

Experimental setups: We implement a temperature controlled optical setup for the frequency comb generation. The spectral tunable range of our drive laser is 1480 nm to 1640 nm, the maximum output power of our erbium doped fiber amplifier (EDFA, BKtel) in the L-band is 3.16 W (35 dBm). The GMR transmission is measured by using the same tunable laser, swept through its full wavelength tuning range at a speed of 40 nm/s. Accordingly we obtain its dispersion and *Q* factors. A fiber coupled hydrogen cyanide gas cell (HCN-13-100, Wavelength References Inc.) and an unbalanced fiber Mach-Zehnder Interferometer (MZI) are used for calibration. To measure the stability and soliton states of our frequency comb, heterodyne and autocorrelation measurements are implemented. For the heterodyne, a stable CW laser with narrow linewidth (300 kHz, New Focus) is applied as the heterodyne reference for the 1530 nm to 1570 nm beatnotes. For the AC measurement, a zero-GVD fiber made of a 7 m DCF and a 15 m SMF is used to guide the microresonator output to the AC setup with minimal pulse broadening and distortion. More details about the experimental setups are shown in Supplementary Figure S13 to S16.

Soliton-step evolution process in the graphene frequency comb. Complementary to Figure 4 of the main text, Extended Data Figure 4 illustrates the soliton states at a gate voltage of -1.2V, for different laser-cavity detunings. With the simultaneous optical and RF spectra measurements, the frequency comb initiates from the Turing pattern (*state i*) into the high-noise patterns (*states ii* and *iii*, with sub-comb competition) prior to settling down into the low-noise soliton comb (*states iv* and *v*). With further detuning, the soliton comb goes back into the high-noise regime (*state vi*) again, due to the thermal instability in the cavity. We then beat the comb lines of the soliton states with a continuous-wave reference laser with two examples for the 8-soliton state (*state iv*) and the 4-soliton state (*state v*). Here the 9th mode and the 56th mode denote the offsets from the pump line. The beatnotes show a more than 40-dB intensity contrast ratio, with a linewidth of 200 kHz, verifying the clean and stable soliton generation.

Data availability. The data that support the findings of this study are available from the corresponding author on reasonable request.

Extended Data Figure 1 | Measured gate-tunable coupling and dispersions in a GMR. a, Dips at ≈ 1600 nm, with different V_G. **b,** Correlation of the roundtrip transmissions and the bus transmissions for the resonator, obeying $T = (\alpha - |t|)^2 / (\alpha - \alpha|t|)^2$. Here 1-$\alpha$ is the cavity loss per round trip, and 1-t is the bus to cavity coupling rate. In our experiment, the graphene ring resonator is under-coupled originally, as the blue dot shows. **c,** GVD in range of 1500 to 1700 nm. Here the curves show the calculated results while dots show measured data. **d,** Calculated TOD in range of 1500 to 1700 nm.

Extended Data Figure 2 | Comparative optical transmissions of the heterogeneous graphene-nitride ring. a, Spectral transmission of the silicon nitride ring resonator under the silica overcladding. **b,** Spectral transmission of the silicon nitride ring resonator after buffer-oxide-etching to remove the silica overcladding. **c,** Spectral transmission of the graphene/ion-gel based nitride ring resonator, heavily *p*-doped (V_G = -2 V). **d,** Loaded *Q* factor around 1600 nm, changes from 1.58×10^6 to 1.04×10^6 with the heavily *p*-doped graphene on a section of the ring. **e,** FSRs, which is sensitive to the geometry modification. **f,** Mode non-equidistances, D_2. **d** to **e** are measured at λ = 1600 nm. In this figure the error bars denote the typical system error.

Extended Data Figure 3 | An implementation of the graphene primary frequency comb gate-modulation. a, Method to measure the modulated comb. Keeping bias V_G = -1.2 V, we control the laser-cavity detuning to generate a primary comb such as the grey spectrum shown here. To filter off 1600 nm CW pump, we apply a C-band filter, selecting the comb lines in C-band only. A signal generator (maximum amplitude of 2 V, HP3312) is applied to modulate the gate voltage between -1.2 V and -1.8 V. In this process, primary comb lines in the filter window are modulated by the gate signal – such a modulation is monitored by using oscilloscope (500 MHz, Rigol DS1054) and ESA (3 GHz, Agilent CXA9000A). **b,** Examples of RF spectra of the modulated combs, filtered by a 1530 nm to 1570 nm optical filter. The radio bandwidth of the ESA is set as 80 kHz.

Extended Data Figure 4 | Example measurements of the graphene soliton comb formation. a, Under V_G = -1.2 V (Fermi level of 0.59 eV), when λ_p tuned from 1600.00

nm to 1600.23 nm, the Kerr frequency comb is generated gradually. When λ_p is tuned between 1600.15 nm and 1600.19 nm, two multi-soliton states with low phase noise are achieved (state *iv* and *v*). **b**, Corresponding RF amplitude noise of the six states. In **a** and **b**, the pump power is kept at 34.5 dBm. Cherenkov radiation of the multi-soliton comb is narrow and sharp. **c,** Zoom-in of the 8-soliton crystal spectrum, the FSR changes from 89 GHz to 718 GHz, due to the soliton crystal based longitude mode interaction. **d,** Beatnote for the comb lines of the 8-soliton state (red; 9th comb line offset from the pump) and the 4-soliton state (green; 56th comb line offset from the pump).

Supplementary Information

Gate-tunable frequency combs in graphene-nitride microresonators

Baicheng Yao[1,2,7*,+], Shu-Wei Huang[1,8*, +], Yuan Liu[3,9,+], Abhinav Kumar Vinod[1,+], Chanyeol Choi[1], Michael Hoff[1], Yongnan Li[1], Mingbin Yu[4,10], Ziying Feng[5], Dim-Lee Kwong[4,6], Yu Huang[3], Yunjiang Rao[2], Xiangfeng Duan[5,*] and Chee Wei Wong[1,*]

[1]*Fang Lu Mesoscopic Optics and Quantum Electronics Laboratory, University of California, Los Angeles, CA, USA*

[2]*Key Laboratory of Optical Fiber Sensing and Communications (Education Ministry of China), University of Electronic Science and Technology of China, Chengdu, China*

[3]*Department of Materials Science and Engineering, University of California, Los Angeles, CA, USA*

[4]*Institute of Microelectronics, Singapore 117685, Singapore*

[5]*Department of Chemistry and Biochemistry, University of California, Los Angeles, CA 90095, USA*

[6]*Institute for Infocomm Research, Singapore, Singapore*

Present Addresses:

[7]*Cambridge Graphene Centre, University of Cambridge, Cambridge, UK*

[8]*Department of Electrical, Computer, and Energy Engineering, University of Colorado Boulder, Boulder, CO, USA*

[9]*School of Physics and Electronics, Hunan University, Changsha, China*

[10]*Shanghai Institute of Microsystem and Information Technology, and Shanghai Industrial Technology Research Institute, Shanghai, China*

* yaobaicheng@uestc.edu.cn; shuwei.huang@colorado.edu; xduan@chem.ucla.edu; cheewei.wong@ucla.edu

[+] B. C. Yao, S. W. Huang, Y. Liu and A. K. Vinod contribute equally in this work.

This Supplementary Information consists of the following sections:

S1. Theoretical analysis and numerical simulations

S1.1. Principle of the dispersion modulation in graphene-silicon nitride microresonator

The carrier density of graphene is tunable via an external electrical field. Let us start with describing solely the graphene layer. During the gate tuning process, conductivity of graphene is modulated, which is written as [S1, S2]:

$$\sigma_g(f, E_F, \tau, T) = \sigma_{g,intra} + \sigma_{g,inter} = \frac{ie^2(2\pi f - i/\tau)}{\pi\hbar^2}\left\{\frac{1}{\left(2\pi f+\frac{i}{\tau}\right)^2}\int_0^\infty \varepsilon\left[\frac{\partial f_d(\epsilon)}{\partial\epsilon} - \frac{\partial f_d(-\epsilon)}{\partial\epsilon}\right]d\epsilon - \int_0^\infty\left[\frac{f_d(-\epsilon)-f_d(\epsilon)}{(2\pi f+i/\tau)^2-4(\epsilon/\hbar)^2}\right]d\epsilon\right\} \tag{S1-A}$$

Specifically,

$$\sigma_{g,intra} = \frac{ie^2E_F}{\pi\hbar(2\pi f+\frac{i}{\tau})} \tag{S1-B}$$

$$\sigma_{g,inter} = \frac{ie^2E_F}{4\pi\hbar}ln\left[\frac{2|E_F|-\hbar(2\pi f+\frac{i}{\tau})}{2|E_F|+\hbar(2\pi f+\frac{i}{\tau})}\right] \tag{S1-C}$$

Here E_F is the quasi Fermi level, directly determined by the external bias. f is the optical frequency, $\tau \approx 10^{-13}$ s is the carrier relaxation lifetime, T is the temperature, $f_d(\epsilon) = \{exp[(\epsilon-\mu)/k_BT]+1\}^{-1}$ is the Fermi-Dirac distribution, $\hbar = 1.05\times10^{-34}$ eV·s is the reduced Planck constant,

$k_B = 1.3806505\times10^{-23}J/\mathrm{K}$ is the Boltzmann's constant, and $e = -1.6\times10^{-19}C$ is the unit charge. Treating graphene as an ultrathin optical media with sheet conductivity, its effective permittivity and refractive index is determined by its complex conductivity [S3, S4, S5]:

$$\begin{cases} \epsilon_g = \dfrac{-\sigma_{g,i}+i\sigma_{g,r}}{2\pi f\Delta} \\ \left(n_{g,r}+in_{g,i}\right)^2 = \epsilon_{g,r}+i\epsilon_{g,i} \end{cases} \tag{S2}$$

For the media mode, $n_{g,r} > 0$ and we get the values of $n_{g,r}$ and $n_{g,i}$ as

$$\begin{cases} n_{g,r} = \dfrac{2\epsilon_{g,r}\left(\frac{\epsilon_{g,r}}{2}+\frac{\sqrt{\epsilon_{g,r}{}^2-\epsilon_{g,i}{}^2}}{2}\right)^{1/2}-2\left(\frac{\epsilon_{g,r}}{2}+\frac{\sqrt{\epsilon_{g,r}{}^2-\epsilon_{g,i}{}^2}}{2}\right)^{3/2}}{\epsilon_{g,i}} \\ n_{g,i} = \left(\dfrac{\sqrt{\epsilon_{g,r}{}^2+\epsilon_{g,i}{}^2}}{2}-\dfrac{\epsilon_{g,r}}{2}\right)^{1/2} \end{cases} \tag{S3}$$

For propagating light, $n_{g,r}$ influences the phase velocity while $n_{g,i}$ refers to the propagation loss [S6]. Based on the dispersion $n_g(f, \mu)$, the gate-tunable GVD parameter of graphene D_g could be calculated:

$$\beta_m = \left(\frac{d^m\beta}{d\omega^m}\right) \tag{S4}$$

$$D_g = -\frac{2\pi c}{\lambda^2}\beta_2 = -\frac{\lambda}{c}\frac{d^2n_{g,r}}{d\lambda^2} \tag{S5}$$

Here $\omega = 2\pi c/\lambda$, m is the order, β_2 is the GVD and β_3 is the TOD. Figure S1 plots the calculated spectra of ϵ_g, n_g and D_g, for a series of Fermi levels. With increasing Fermi level, the graphene dispersion is sizably tuned, from anomalous to normal, and then finally back to anomalous.

In this work, atomic layer graphene is deposited onto the silicon nitride waveguides. Standard optical parameters of silicon nitride waveguide are calculated in Figure S2. Figure S2a, S2b and S2c shows the group velocities, the group velocity dispersions (GVD; β_2) and the third order dispersions (TOD; β_3) of the silicon nitride waveguides. All the results are calculated based on TE polarization. Here the numbers marked in the figures are the width of the silicon nitride waveguides, with a fixed height 0.8 μm. The blue curves highlight the results of width = 1.2 μm, which is applied in our experiment.

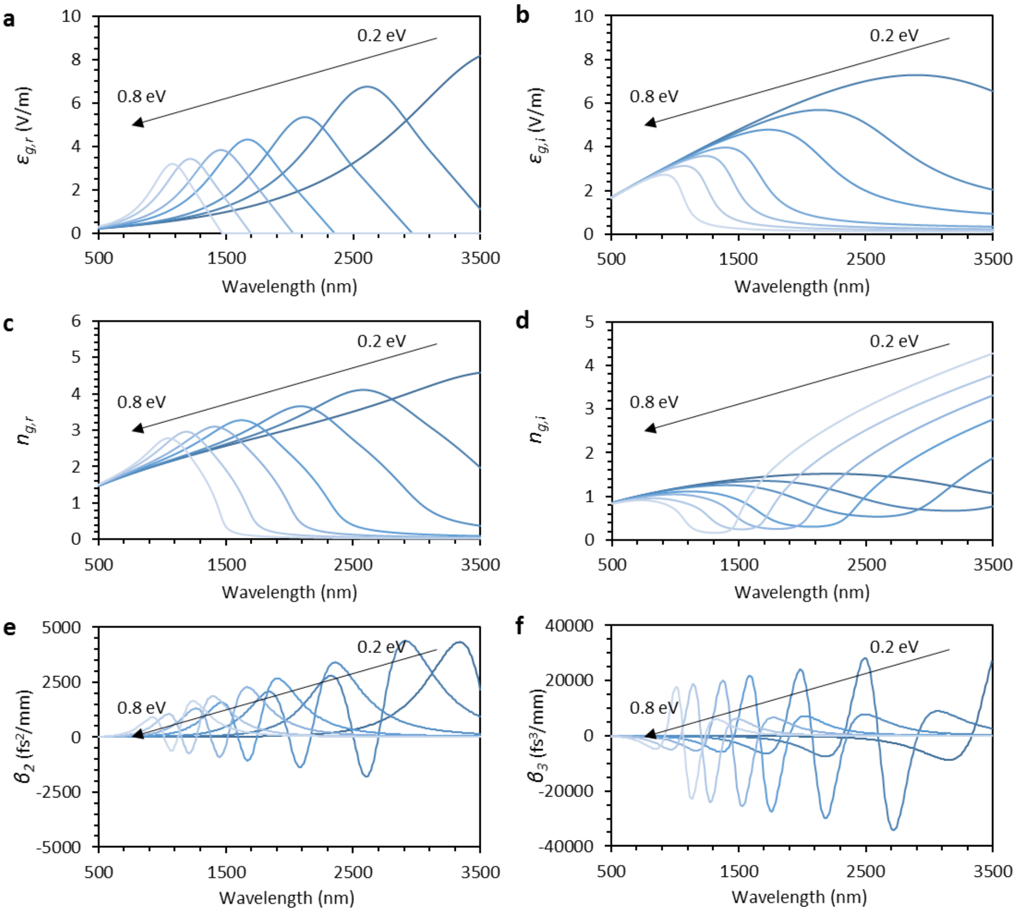

Figure S1 | Gate-tunable dispersion of graphene. a and **b,** Real part and imaginary part of the graphene permittivity, under varying from 0.2 eV to 0.8 eV (labeled from dark blue to light blue). **c** and **d,** Real part and imaginary part of the refractive index. **e,** Group velocity dispersion (GVD). **f,** Third-order dispersion (TOD).

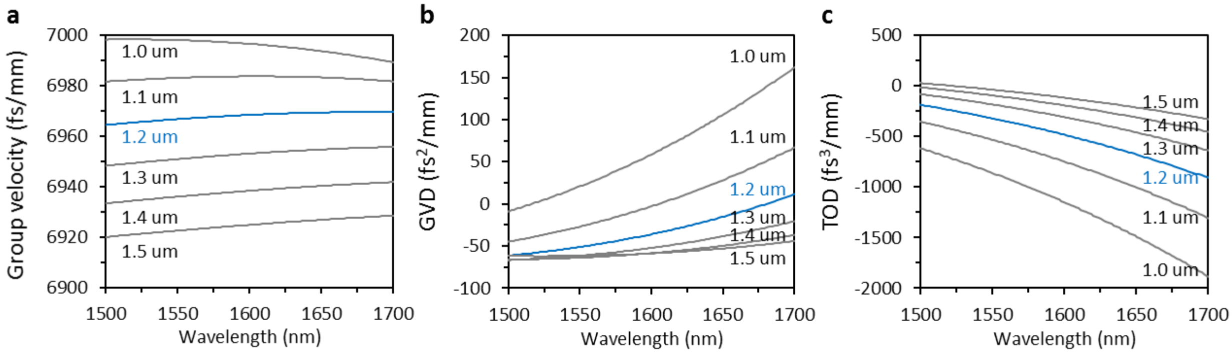

Figure S2 | Calculated optical properties of the silicon nitride waveguide, for TE polarization. **a,** group velocities. **b,** GVD. **c,** TOD. Waveguide height: 0.8 μm; waveguide width varies from 1.0 μm to 1.5 μm.

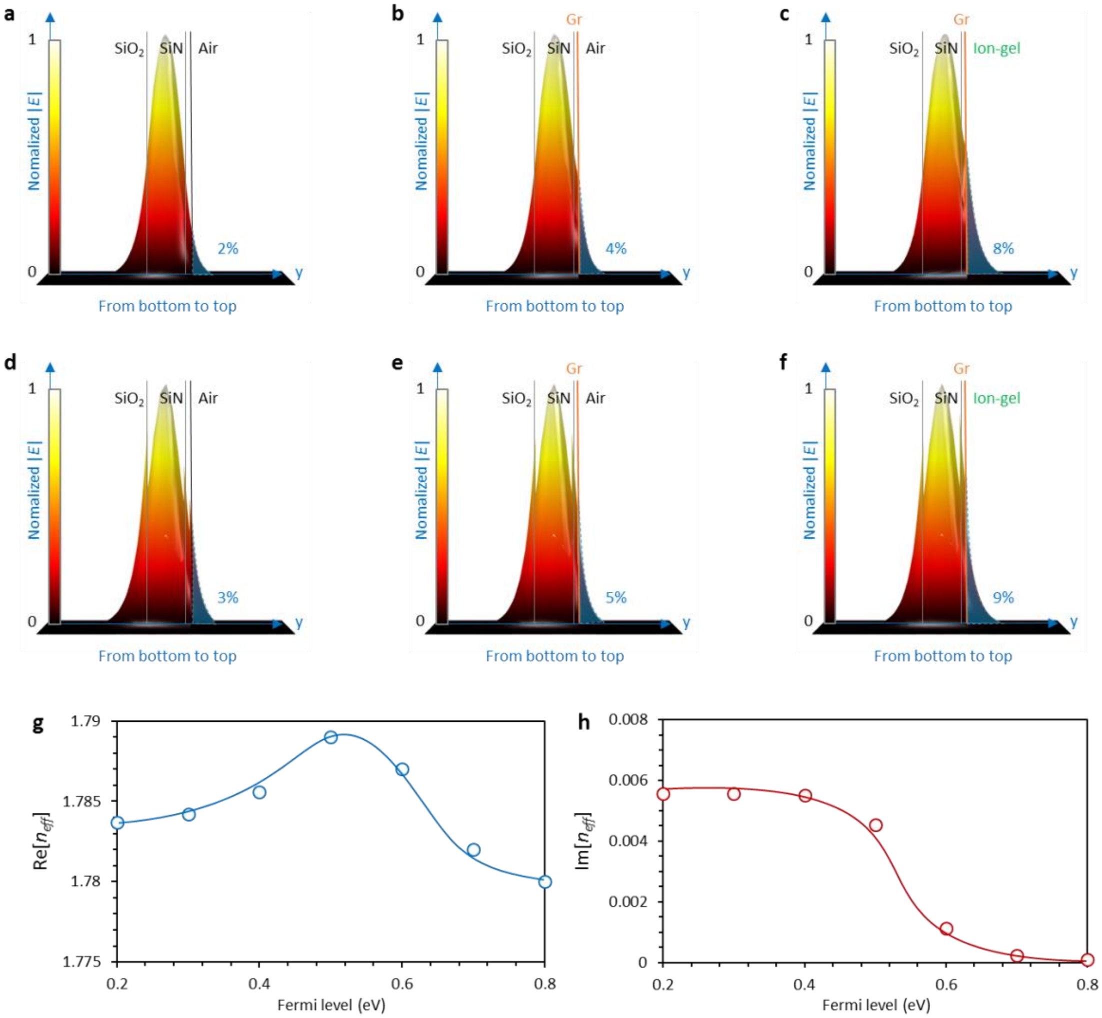

Figure S3 | Modelled |*E*|-field distributions of the heterogeneous graphene-nitride structure. a-c, TE_{01} mode distributions in the top etched nitride waveguide, after the graphene deposition, and after the ion-gel coverage. **d-f,** TM_{01} mode distributions in the top etched nitride waveguide, after the graphene deposition, and after the ion-gel coverage. **g-h,** During Fermi level increases from 0.2 eV to 0.8 eV, real part and imaginary part of the fundamental TE_{01} mode. In these simulations, Si_3N_4 cross-sectional size is 1200 × 800 nm^2.

By using the finite-element method, Figure S3 demonstrates the simulated |*E*|-field distributions of the silicon nitride waveguides with 1200 × 800 nm^2 core, for optical wavelength 1600 nm. Figure S3a to S3c are the simulated results of the TE_{01} mode, while Figure S3d to S3f show the TM_{01} mode. In this simulation, we fix the parameters: graphene Fermi level at 0.5 eV, graphene thickness of 0.5 nm, ion-gel thickness of 1 μm with refractive index of 1.420 [S7], silicon nitride refractive index of 1.996, silica refractive index of 1.462. Determined by the electromagnetic boundary conditions, distributions of the TM_{01} mode are not continuous along the *y*-axis. For TE_{01} mode, before graphene deposition, ≈ 2% mode intensity distribute in the air. Afterwards, determined by the high index of graphene (3.27+i0.65 at 0.5 eV), more mode energy (≈ 4%) distributes outside, enhancing the light-graphene interaction. Finally, by covering the ion-gel on the graphene, we further increase the evanescent field distribution, up to ≈ 8% overlapping above the graphene sheet. Spatial distributions of the TM_{01} mode are similar. Enhanced by the graphene and ion-gel, mode field intensity out of the nitride/oxide waveguide increases from ≈ 3% to ≈ 9%. However, determined by the polarization dependent loss induced by scattering and absorption, *Q* factor of the TM_{01} mode is much lower than the TE_{01} mode. Furthermore, by modulating the n_g via gate tuning, effective index of the hybrid waveguide n_{eff} changes correspondingly [S8, S9]. Figure 3g and S3h plots the calculated effective index of the fundamental TE_{01} mode, at 1600 nm wavelength in the hybrid waveguide during the graphene Fermi level tuning from 0.2 eV to 0.8 eV.

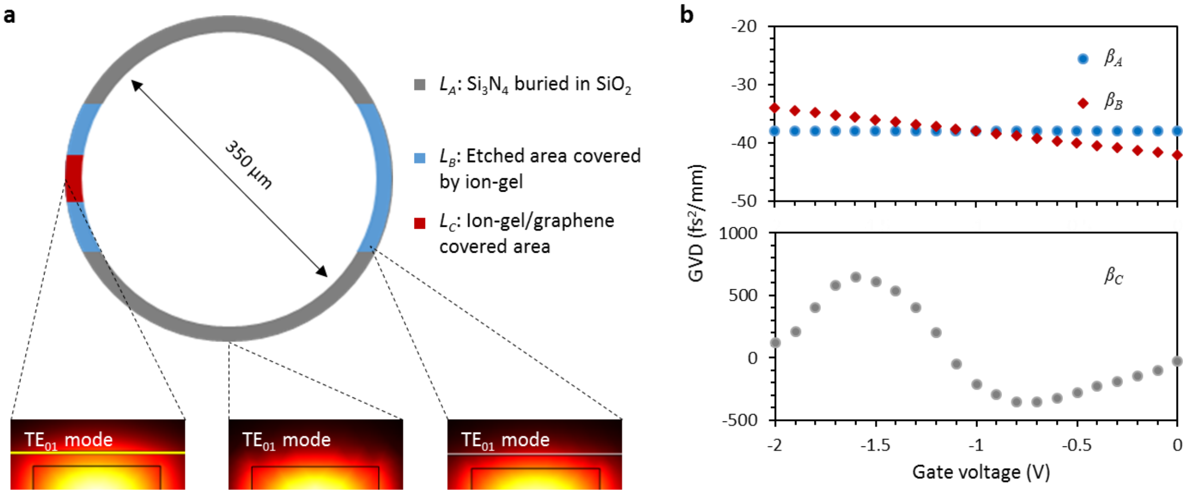

Figure S4 | Calculation of the microresonator dispersion. a, Top-view geometry of the graphene based microresonator. Three sections are marked: L_A, the nitride core buried in oxide cladding, L_B, the etched area covered by Ion-gel, L_C, the graphene heterostructured area. Inset: the TE_{01} mode in the 3 sections has different spatial patterns. **b,** Calculated GVDs of the 3 sections.

To calculate the dispersion of the whole microresonator at 1600 nm wavelength, Figure S4a shows the segmentation of the geometry. Arc lengths of L_A, L_B and L_C are ≈ 790 µm, ≈ 220 µm, and ≈ 90 µm respectively. We denote the respective GVDs as β_A, β_B, and β_C, separately calculated with *COMSOL*. Total dispersion of the microring resonator is thus written as $\beta_2 = (\beta_A L_A + \beta_B L_B + \beta_C L_C) / (L_A + L_B + L_C)$. Figure S4b plots the calculated β_A, β_B, and β_C during the gate tuning operation, with the below three observations: **(1)** gate voltage does not affect β_A, which is kept constant around -38 fs^2/mm. **(2)** due to the ions motion and thermal heating of the ion-gel, the refractive index of the L_B section decreases slightly by ≈ 0.001 at 1600 nm [S10], with β_B increasing slightly from ≈ -42 fs^2/mm to ≈ -34 fs^2/mm in linear approximation, under gate voltage tuning from 0 V to -2 V. Compared to graphene, such a GVD modification from the ion gel and nitride temperature variation is more than two orders-of-magnitude smaller. **(3)** for the graphene/ion-gel heterostructured section, β_C oscillates dramatically compared to β_A and β_B.

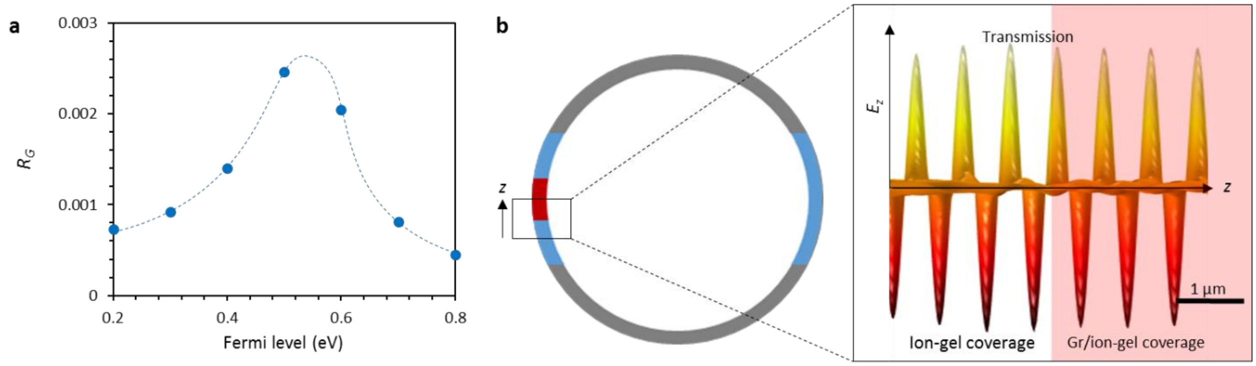

Figure S5 | Heterogeneous graphene-nitride structure induced Fresnel reflection. a, Calculated reflection ratio at the boundary of ion-gel nitride section / heterogeneous graphene-nitride, changing in range of 0.08% to 0.24% with Fermi level tuning and gate modulation. **b,** Simulated spatial waveform in the microresonator. Here *z* shows the clockwise direction.

Reflection or backward scattering in high *Q* microresonators may cause standing-wave modes [S11,S12,S13]. For frequency comb generations pumped at high power, strong standing waves which may induce hole-burning should be avoided. In our graphene heterostructured nitride microresonator, because graphene's thickness is only ≈ 5Å and the single-mode (TE_{01}) wavevector is parallel to the graphene sheet, the scattering is negligibly weak. For example, we do not observed mode-splitting in transmission and high-resolution spectral measurements on our high *Q* microresonator measurements, aided by the nitride waveguide uniformity. To further support this, Figure S5a shows our calculated reflection ratios of the TE_{01} mode, R_G, based on Fresnel equation. Determined by the Fermi level of graphene, R_G changes via gate tuning, with the highest value of R_G at 0.24% for the graphene Fermi level $|E_F|$ at ≈ 0.5 eV. Figure S5b further simulates a waveform example (via COMSOL) along the microresonator, for $|E_F| = 0.5$ eV, with little reflections at the graphene/ion-gel interface.

S1.2. Kerr comb generation and dispersion modulation in graphene microring resonator.

Considering that light propagates predominantly in the TE_{01} mode, Kerr comb generation in time domain is governed by the well-known nonlinear Schrodinger equation (NLSE) in graphene ring resonator [S14, S15],

$$\frac{\partial E(z,t)}{\partial z} = \frac{\alpha_L}{2}E + i\sum_{k>1}\frac{\beta_k}{k!}\left[i\frac{\partial}{\partial t}\right]^k E + i\gamma|E|^2 E \tag{S6}$$

Here α_L is the linear absorption coefficient of the resonator, $\beta_k = d^k\beta/d\omega^k \mid (\omega=\omega_0)$ are the dispersion coefficients, associated with the Taylor series expansion of the propagation constant β at center frequency ω_0. $\gamma = n_2\omega_0/cA_{eff}$ is the nonlinearity coefficient with the nonlinear refractive index n_2 and sectional-view effective modal area of the waveguide A_{eff}. Considering the comb dynamics in the cavity round trip, the NSLE is expressed in time domain [S16],

$$t_R\frac{\partial E(T,t)}{\partial T} = \left[-\alpha - i\delta_0 + iL\sum_{k>1}\frac{\beta_k}{k!}\left[i\frac{\partial}{\partial t}\right]^k E + i\gamma L|E|^2\right]E + \sqrt{\theta}E_{in} \tag{S7}$$

Here θ is the transmission coefficient, L the is roundtrip length of the resonator, E_{in} is the input field, t_R is the roundtrip time, $\alpha = (\alpha_L+\theta)/2$ shows the total cavity loss, δ_0 is the detuning, T is the real cavity time, determined by the roundtrip as well. By using Fourier transform, Eq. (S7) could be written and solvable in frequency domain. With increasing round trips, comb lines are generated in spectrum, as shown in Figure S6 schematically. Specifically, the intensities of the comb lines are determined by the nonlinearity coefficient γ and GVD β_2, the comb line spacing is affected by the FSR, and comb bandwidth is primarily influenced by both β_2 and β_3.

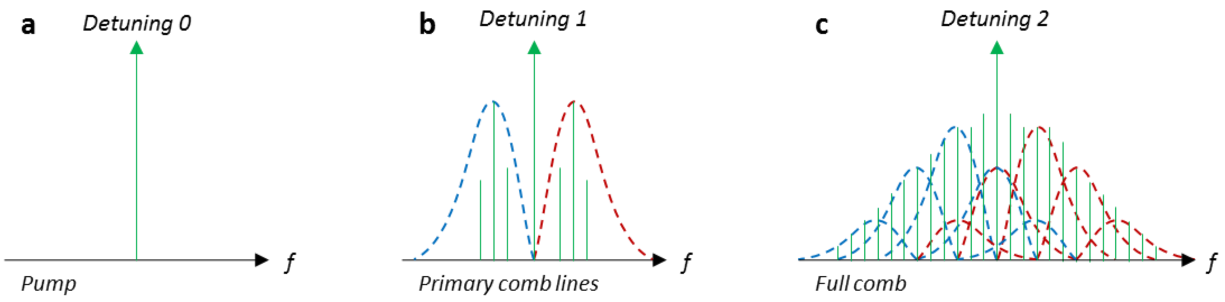

Figure S6 | Process of comb generation. a, Initially only the pump line shows in the spectrum. **b,** By changing the detuning, primary comb lines begin to appear. **c,** When the detuning meets the phase matching conditions well, the comb lines grow fully in the spectrum.

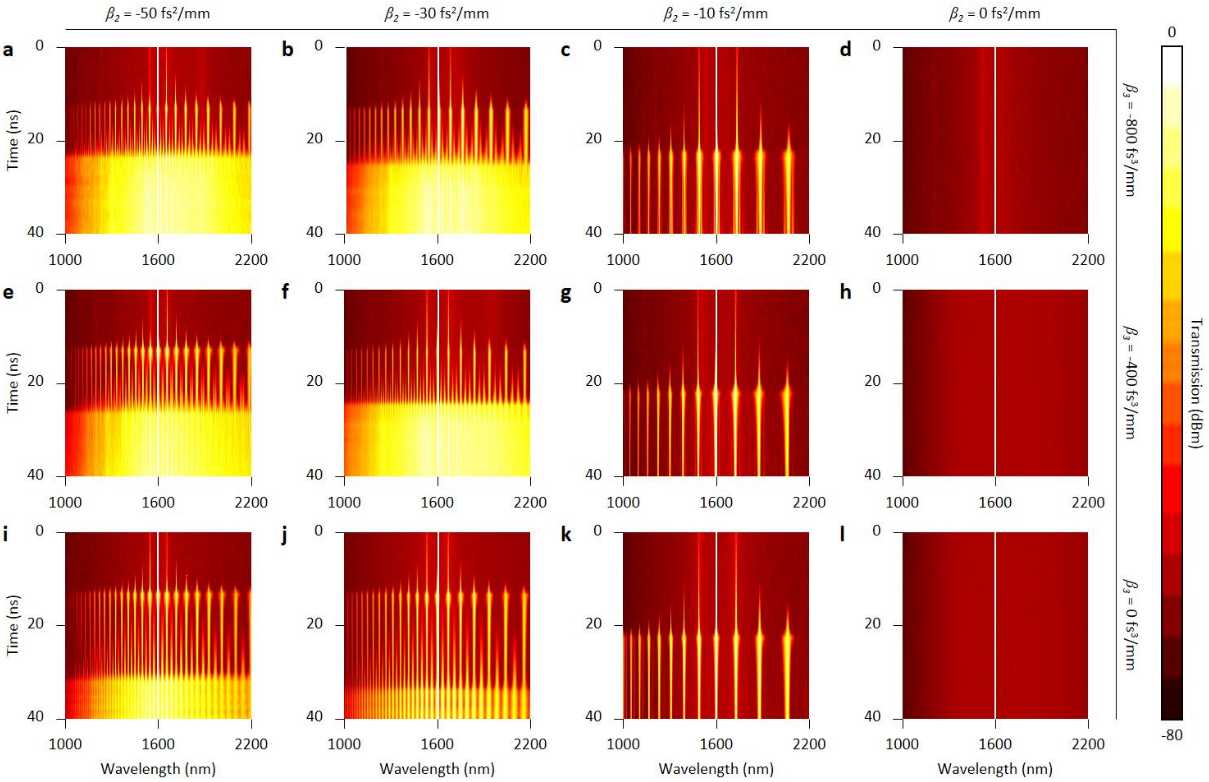

Figure S7 | Comb generation under different operating conditions. Horizon row panels: GVD increases from -50 fs^2/mm to 0 fs^2/mm. Vertical column panels: TOD increases from -800 fs^3/mm to 0 fs^3/mm.

Based on the phase matching condition, Kerr gain and energy balance, Eq. (S8) shows these relationships approximately [S17]:

$$\begin{cases} \kappa_j = \Delta k_j + 2\gamma P_j \\ P_j = \sum_{i\neq j} P_i\sqrt{4(\gamma P_i)^2-(\kappa_i/2)^2} \\ P_0 = \sum P_j \end{cases} \tag{S8}$$

In this equation, κ_j is the phase mismatching, $\Delta k_j = \Delta k_{j,Ring} + \Delta k_{j,g}$ is the dispersion based phase mismatching, which is contributed by both the graphene and the silicon nitride ring, P_j is the power. For these parameters, j is the mode number of a comb line, and j = 0 means the input pump. This equation tells us that the dispersion modulation could be obviously measured in spectrum via checking the primary comb locations. Particularly, we can write the relative frequency difference of the generated primary lines to the pumped mode as [S18] as:

$$\Delta f = f_{FSR}\sqrt{\frac{\kappa}{\beta_2}\left(\sqrt{\frac{P_p}{P_{th}}-1}+1\right)} \tag{S9}$$

Here f_{FSR} is the spectral width of the FSR, β_2 is the group velocity dispersion, P_p is the pump power, and P_{th} is the threshold power. It tells that the dispersion modulation is directly captured by the movement of the primary comb lines. By scanning the detuning in a short range (5 μrad) in 0 to 40 ns, we simulate the comb generation processes of our graphene based nitride microresonator, under different β_2 and β_3, as shown in Figure S7. These simulations show the complete process how full combs are formed from the pump.

Particularly, with a fixed TOD at -800 fs^3/mm, we plot the simulated comb generation process in Figure S8. Figure S8a and S8b show the primary comb lines and the full comb at β_2 = -100 fs^2/mm. Figure S8c and S8d show the primary comb lines and the full comb at β_2 = -80 fs^2/mm. Figure S8e and S8f show the primary comb lines and the full comb at β_2 = -50 fs^2/mm. A smaller GVD results in the primary comb lines farther from the central pump, which is also observed in experiment. In above simulations, we fix the effective mode area as a 0.8 μm^2 cross-section, a pump wavelength without detuning of 1600 nm, a cavity length of the ring a 1.57 mm, a loaded quality factor of 2×10^6, and a launched power of 2 W. Referring the gate voltage based dispersion tuning, Figure S8g maps the generation of primary comb lines under V_G = -1 V, -1.2 V and -1.5 V, corresponding to Figure 3 of the main text.

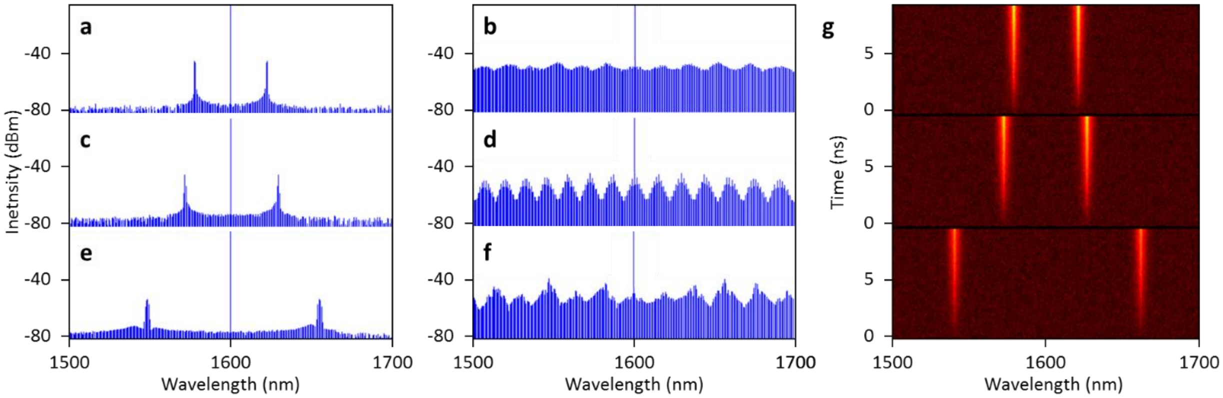

Figure S8 | Charge-tunable nonlinear microresonator comb lines. a, b, and **c,** Primary comb lines when β_2 = -100 fs^2/mm, -80 fs^2/mm, -and -50 fs^2/mm. **d**, **e,** and **f,** Full comb spectra when β_2 = -100 fs^2/mm, -80 fs^2/mm, and -50 fs^2/mm. Here the TOD is fixed at -800 fs^3/mm. **g,** gate voltage virus primary comb line location.

S1.3. Third-order nonlinearity of graphene.

It is known that graphene has a large optical nonlinearity, contributing to the four-wave mixing process [S19, S20]. The nonlinear parameter γ of the graphene ring resonator could be written as $\gamma = 3Re[2\pi f\chi^{(3)}/n_{eff}cA_{eff}]$, wherein $\chi^{(3)}$ is the third-order nonlinear susceptibility and A_{eff} is the effective mode area [S21]. Figure S9 shows the γ of graphene, the silicon nitride core, and the hybrid waveguide respectively. For $|E_F| > 0.3$ eV, a further higher Fermi level brings a lower γ [S22, S23]. Compared to silicon nitride, the third-order nonlinearity parameter of graphene is over 2 orders-of-magnitude higher. However, graphene only affects the evanescent field of the ring and hence the overall field-averaged enhancement with graphene is only slightly larger than nitride in this case: when E_F is tuned higher than 0.6 eV, γ of the hybrid waveguide is $\approx 3\times10^3$ $m^{-1}W^{-1}$.

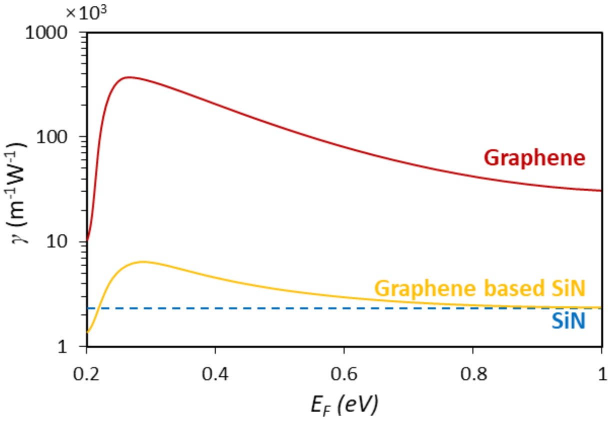

Figure S9 | Heterogeneous graphene-nitride third-order nonlinear susceptibility. Red solid line: graphene; blue dashed line: silicon nitride; gold solid line: graphene-silicon nitride hybrid.

S1.4. Cherenkov radiation and soliton generation.

Optical Cherenkov radiation, also known as dispersive wave, describes the radiation from a canonical soliton when perturbed by higher-order dispersions [S24, S25, S26]. As shown in Figure 1, not only the GVD, β_2, but also the TOD, β_3, can be tuned by changing the gate voltage to the graphene layer. Thus, the spectral peak of the Cherenkov radiation is also gate-tunable in the graphene-nitride microresonators.

For efficient energy conversion from the canonical soliton to the optical Cherenkov radiation, their propagation constants have to be matched and thus

$$\beta_s = \beta_0 + \beta_1(\omega_D - \omega_S) + \gamma P/2 = \beta_0 + \beta_1(\omega_D - \omega_S) + \sum_{N\geq 2}\frac{\beta_N(\omega_D-\omega_S)^N}{N!} = \beta_D \qquad \text{(S10)}$$

, where β_S and β_D are the propagation constants of the canonical soliton and the Cherenkov radiation respectively, γ is the nonlinear coefficient, P is the pump power, ω_S and ω_D are the center frequencies of the canonical soliton and the Cherenkov radiation respectively. Assuming the Cherenkov radiation is spectrally well separated from the canonical soliton, $\gamma P \ll \beta_2(\omega_D - \omega_S)^2$, the phase matching condition can be simplified as

$$f_D = f_S + \frac{3}{2\pi}\frac{|\beta_2|}{\beta_3} \tag{S11}$$

In the Kerr comb evolution, Turing patterns[S27, S28], chaotic states [S29] and soliton states [S30, S31] appear successively. Taking advantage of the Lugiato-Lefever mean-field model [S32], we show the difference of the Turing patterns before chaotic state and the finally formed solitons after chaotic state in Figure S10. We note that when the TOD higher than -300 fs^3/mm, it is hard to generate single soliton state by using a 600 mW on-chip pump. During the pulse evolution, multi-soliton states with versatile pulse operations are essential processes, which are also timely stable, having shown great potential in applications such as harmonic sources and ultrafast information-processes [S33, S34, S35].

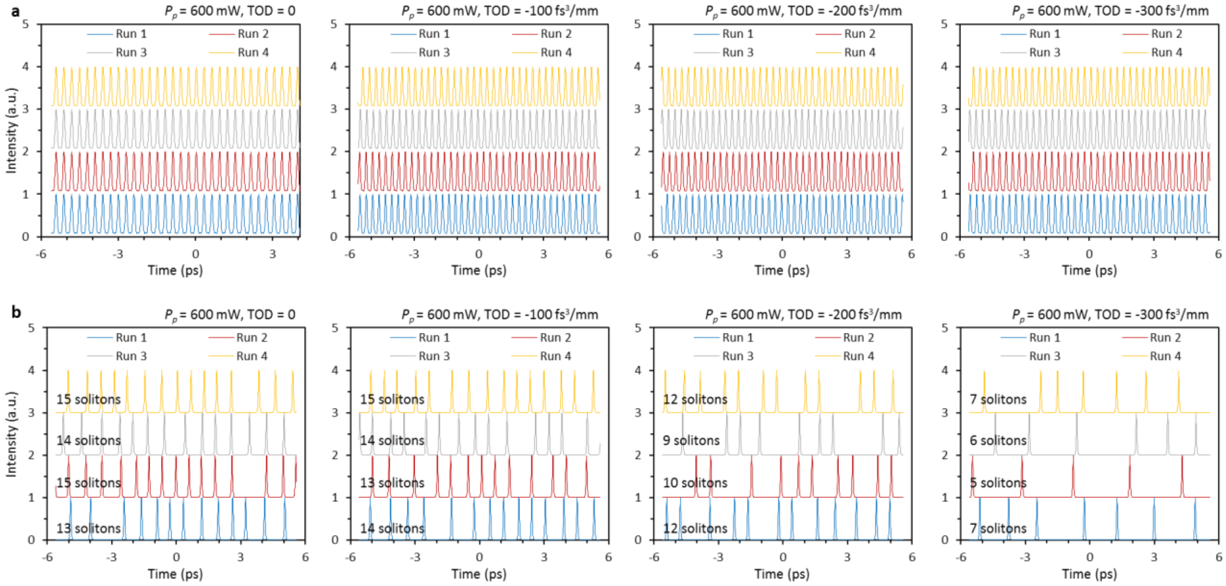

Figure S10. Simulated results of the Turing patterns and soliton generations. a, Turing patterns. **b,** Final formations of the multi-solitons. In the simulations, we use on-chip pump power 600 mW, GVD -30 fs^2/mm, intrinsic Q factor 1.061 × 10^6, cavity length 1.1 mm, effective mode area 1 μm^2, central wavelength 1600 nm.

Moreover, we demonstrate the simulated results of the Cherenkov soliton formations in Figure S11. Here we use TOD varying from -300 fs^3/mm to -500 fs^3/mm. Figure S10a to S10c plot the temporal profiles of the final soliton formations. Figure S10d to S10f show the statistical histograms. For TOD at -300 fs^3/mm, -400 fs^3/mm and -500 fs^3/mm, possibility of single soliton generation is estimated 0%, 44%, and 67%, respectively. The simulated results imply that for a specific GMR, single soliton tends to appear with a larger TOD and a larger pump power. For the GMR, however, a larger TOD brings higher sensitivity of GVD spectrally, which then increases the difficulty for single soliton thermal stabilization.

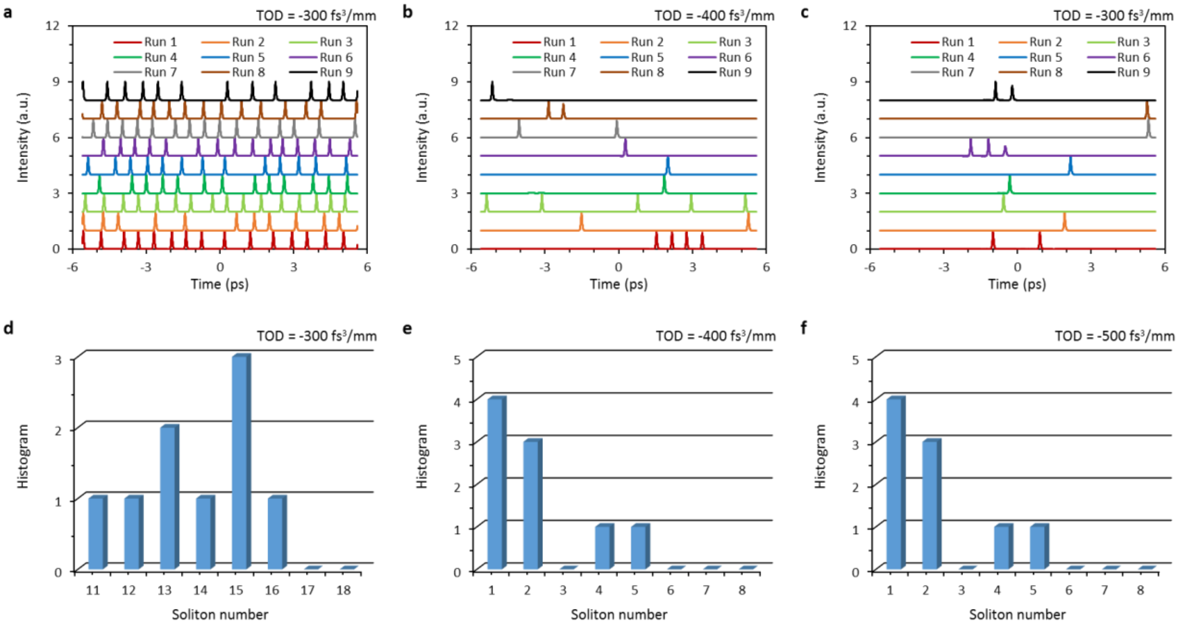

Figure S11. Numerical studies and distribution of the single-soliton states. a to **c,** Modelled soliton structures for TOD at -300 fs^3/mm, -400 fs^3/mm, and -500 fs^3/mm respectively. **d** to **f,** Occurrence distributions of the soliton numbers. In the simulations, we use a GVD of -30 fs^2/mm, an intrinsic Q factor of 1.06×10^6, a cavity length of 1.1 mm, an effective mode area of 1 μm^2, and a central pump wavelength of 1600 nm.

S2. Fabrication and baseline characterization

Figure S12 shows the fabrication process flow of the graphene-based Si_3N_4 microresonators. The microresonator has a cross-sectional 1000 × 800 nm^2 bus waveguide and a cross-sectional 1200 × 800 nm^2 core for the ring. Above the ring, there is 2500 nm thick SiO_2. First, by using standard photo-lithography followed by buffered oxide etching (7 mins), we create a photoresist window above the ring and etched the SiO_2 to 100 nm ~ 400 nm thick for better graphene-light interaction and chromatic dispersion management.

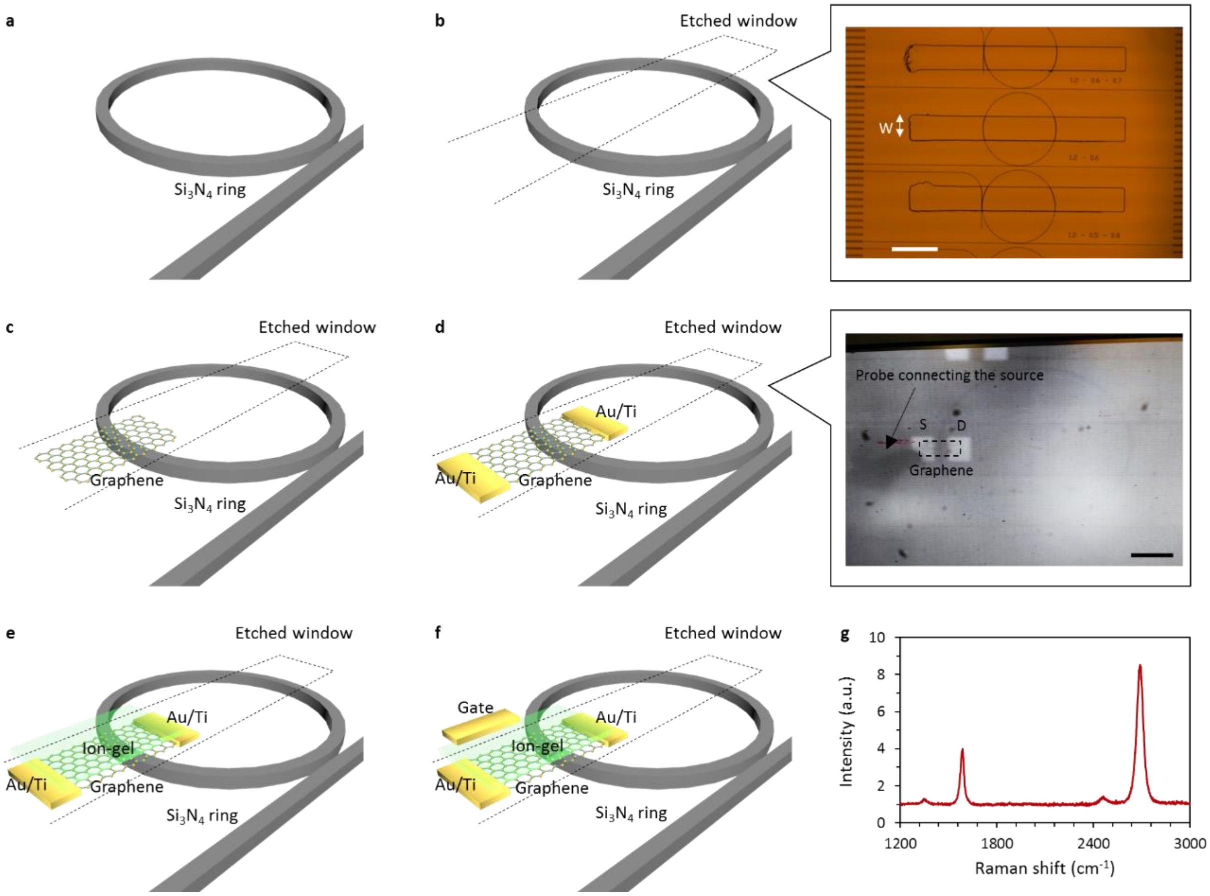

Figure S12 | Device fabrication process. a, Schematics of silicon nitride ring resonator buried in silica cladding. **b,** Schematics (left) and the top-view microscope image (right) of the chip after photolithography and oxide etching. Scale bar: 300 μm. **c,** Schematic of a monolayer graphene transferred and patterned in the etched window. **d,** Schematic (left) and top view image (right) of the device with source-drain electrodes integrated on graphene. Scale bar: 100 μm. **e,** Schematics of graphene source-drain-dielectric with a layer of ionic liquid as the gate dielectric. **f,** Schematics of device structure with gate electrode integrated. **g,** Raman spectrum of the monolayer graphene.

It is noted the edge of the ring need to be well protected by ultra-thick photoresist (~1 mm) to prevent damage from the etching process. Inset of Figure S12b shows the top-view image of the substrate with an etched oxide window. Secondly, we transfer a monolayer graphene on the etched window, followed by photolithography patterning and oxygen plasma etching, as shown in Figure S12c. The graphene layer is grown by low pressure chemical vapor deposition (LPCVD) method on copper substrate and transferred using a modified transfer technique using PPC (polypropylene carbonate) as the protection layer. The LPCVD and PPC transfer here is essential to integrate high quality graphene on top of the ring. Next, as shown in Figure S12d, we deposit source drain electrodes (Ti/Au, 70/100 nm) using photo lithography and e-beam evaporation. Here the size of the pads is 80 μm× 60 μm. Inset of Figure S12d shows the microscope image of this step, with the chip put on the setup. Finally, we integrate ionic liquid (DEME-TFSI (N,N-diethyl-Nmethyl-N-(2-methoxyethyl) ammonium bis (trifluoromethylsulfonyl) imide, from Sigma-Aldrich) as the gate dielectric, resulting an electric double layer graphene transistor with large gate capacitance. Raman spectrum of the monolayer graphene is shown in Figure S12g, indicating the high quality of CVD grown graphene [S36].

S3. Supplementary measurements

S3.1. Experimental setup for the gate-tunable comb generation.

Figure S13a shows the experimental setup for comb generation and modulation. A tunable laser (Santec 710) with tunable range from 1480 nm to 1640 nm serves as the drive laser. It is amplified by an erbium doped fiber amplifier (EDFA, BKtel) in the L-band, working as the pump. In the experiment, the laser is tuned around 1600 nm, and the amplified power is 3.16 W (35 dBm). The pump beam is launched onto the chip via free-space. A polarization controller (PC) and a polarized beam splitter (PBS) are used to ensure the launched light is in the transverse electric (TE) mode. The graphene heterostructured microresonator (GMR) chip is fixed on a chip holder, whose temperature is controlled with a thermoelectric cooler. To tune the comb, the GMR is gated by a pair of electrical probes. For the comb spectra, the output signal is analyzed by an optical spectrum analyzer (Advantest Q8384; Yokogawa AQ6375).

Figure S13b shows the setup to gate the graphene-based resonator chip. Here two probes connect the gate and source separately. The drive laser is launched onto the chip via optimized and matched coupling lens. Figure S9c shows the image of the gated chip under an infrared camera; here the Au/Ti patterns deposited on the chip are the bright spots and the source and drain with graphene are marked by ‘*S*’ and ‘*D*’. A probe inserting in the ion gel (without touching the chip) works as the top gate, marked as ‘*G*’. In addition, here the etched window is marked by the blue dashed box and the silicon nitride resonator is marked by the red dashed ring.

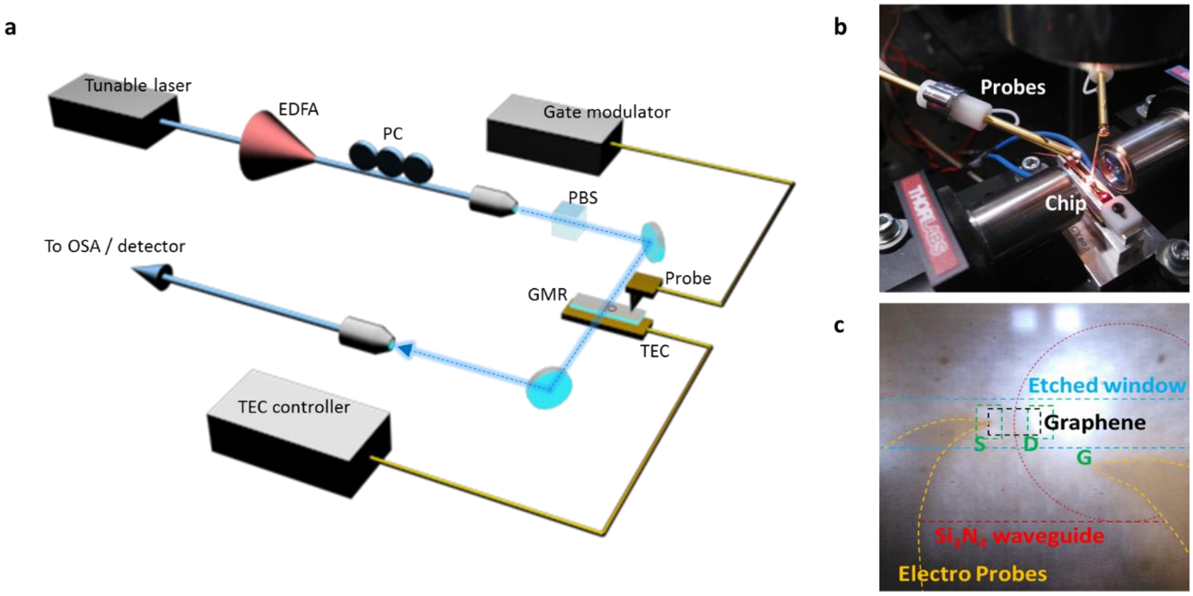

Figure S13 | Experimental arrangement. a, Schematic of the experimental setup. **b,** Probing and aligning the graphene microring resonator chip. **c,** Microscope image of the probed chip in experiment, under an infrared camera. All of the ring resonator is covered by the ion-gel. EDFA: erbium-doped fiber amplifier. PC: polarization controller. PBS: polarization beam splitter. GMR: graphene microring chip. TEC: thermoelectric cooler for chip temperature control.

S3.2. MZI-clocked dispersion measurement, with HCN optical transition referencing.

Figure S14 shows the setup for the graphene resonator transmission and dispersion measurement [S37]. The graphene microring resonator transmission is measured using a tunable laser swept through its full wavelength tuning range at 40 nm/s. Accordingly we can get its dispersion and *Q* factors. For accurate wavelength calibration, 1% of the laser output is directed onto a fiber-coupled hydrogen cyanide gas cell (HCN-13-100, Wavelength References) and then into a photodetector (PD 1). The graphene microring resonator and gas cell transmission are recorded during the laser sweep by a data acquisition system whose sample clock is derived from a photodetector (PD 2), monitoring the laser transmission through an unbalanced fiber Mach-Zehnder interferometer (MZI). The MZI has a determined 40 m path length difference, ensuring a measurement optical frequency sampling resolution of 5 MHz. The absolute wavelength of each sweep is determined by fitting 51 absorption features present in the gas cell transmission to determine their subsample position, assigning them to known traceable wavelengths [S38] and calculating a linear fit in order to determine the full sweep wavelength information. Each resonance is fitted with a Lorentzian lineshape unless a cluster of resonances is deemed too close to achieve a conclusive fit with a single Lorentzian. In that case, an *N*-Lorentzian fit is utilized where *N* is the number of resonances being fitted. The dispersion of the graphene ring resonator is finally determined by analyzing the wavelength dependence of the FSR. In the setup, the graphene microring resonator chip is gated by a probe.

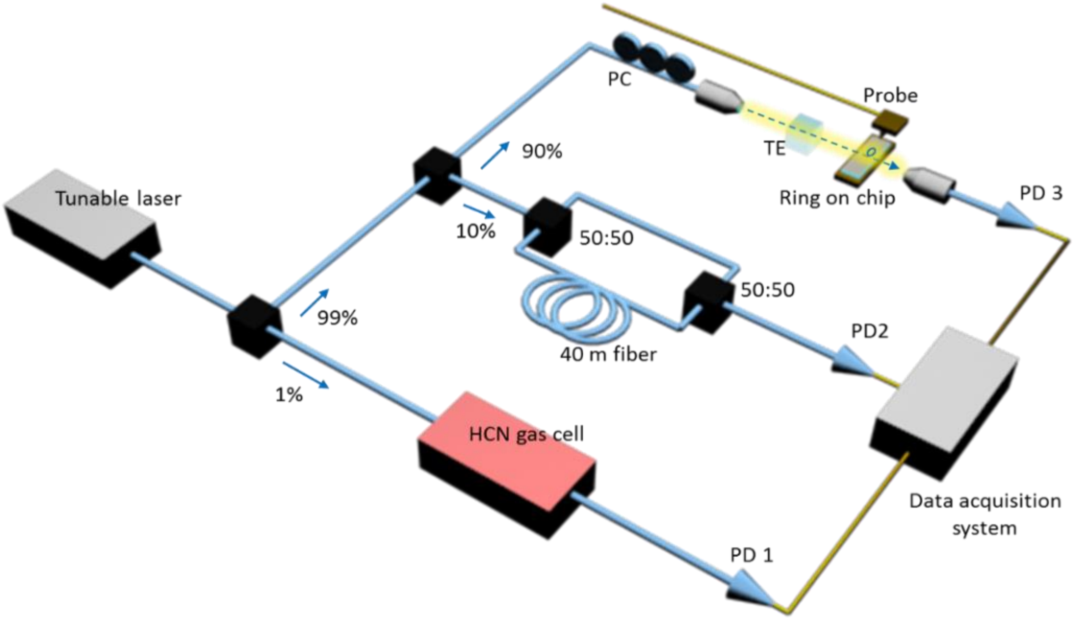

Figure S14 | Setup to quantify the dispersions and *Q* factors of the graphene microring resonators on-chip. The swept input laser is clocked with a highly-imbalanced MZI with 5 MHz optical frequency sampling resolution, and referenced against the optical transitions of a HCN reference gas cell. PC: polarization controller. TE: transverse electric mode. HCN: hydrogen cyanide. PD: photodetector.

S3.3. Heterodyne beat notes and autocorrelation measurements for soliton states.

To measure the stability and soliton states of our frequency comb, Figure S15a shows our optical heterodyne setup. We use a WDM to separate the C-band comb lines (1530 nm – 1570 nm) and the L-band comb lines (1570 nm – 1630 nm) from the pump. The 1570 nm – 1630 nm window is monitored by an OSA (Advantest AQ8384). The 1530 nm – 1570 nm spectrum beats with a stable continuous-wave (CW) laser with a narrow linewidth (300 kHz, New Focus), which serves as the heterodyne reference. A PC is used to optimize the pump polarization. The beatnotes are measured by a 3 GHz RF ESA (Agilent CXA 9000A). The comb signal is also measured in the time-domain, using a built optical intensity autocorrelator (AC). In this part, a 7 meter long dispersion-compensated fiber (DCF) along with a 15 meter long single-mode fiber is used to compensate the GVD, avoiding the pulse broadening. Figure S15b shows the measured AC traces of our graphene based microresonator. With decreasing the pump detuning, we demonstrated the Turing patterns with dense oscillation but low extinction ratio (<3 dB), high noise state, and stable soliton states.

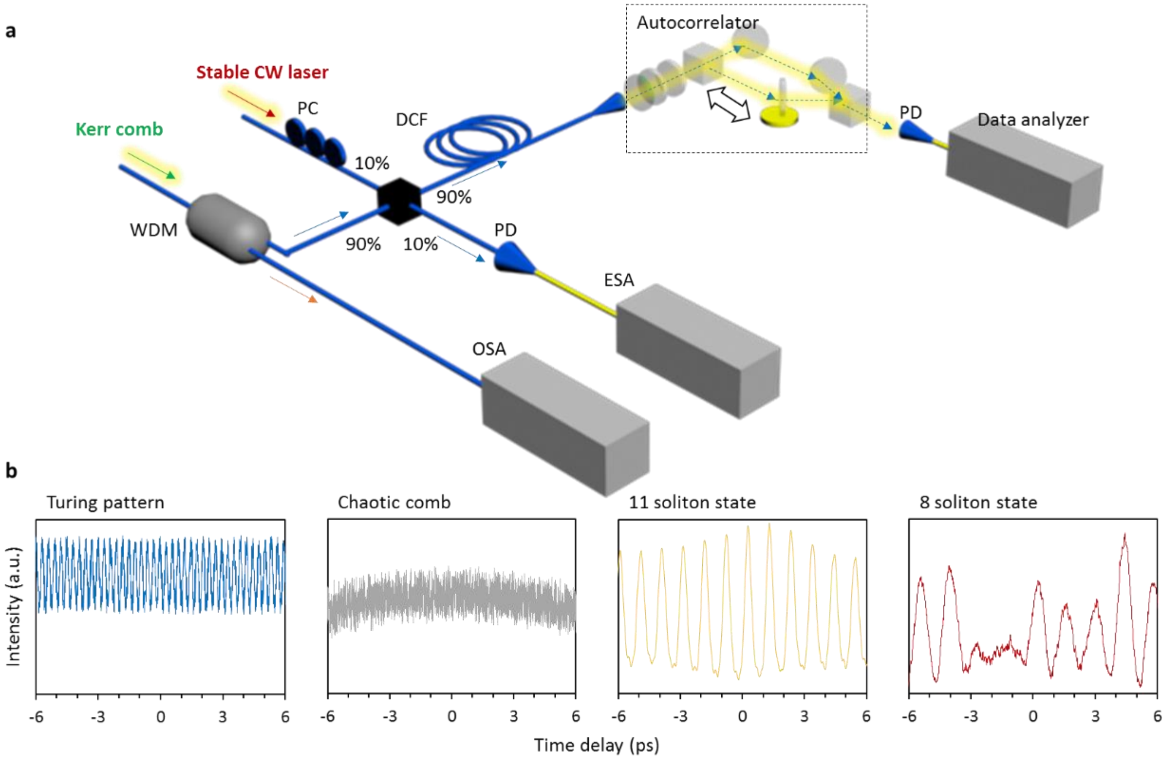

Figure S15 | Measuring the Kerr frequency comb states, with optical heterodyne and autocorrelation (AC). a, Setup: PC: polarization controller. DCF: dispersion-compensated fiber. WDM: wavelength-division multiplexer. PD: photodetector; OSA: Optical spectrum analyzer; ESA: Electric spectrum analyzer. **b,** Measured AC trace samples: from left to right, Turing, high noise, 11 soliton crystal and 8 soliton crystal.

S3.4. Measurement of the dispersion instability due to the ion dielectric.

Figure S16a shows the schematic sectional view when gating the graphene heterostructure. The gate probe is close to the graphene (height < 1 μm) while far away from the nitride core (distance > 10 μm). Mode field distribution ratio around the probes is less than 10^{-4} (Figure S4), hence the carriers in the gate probe can hardly influence the mode field. During the gate voltage tuning, the ions form an electric double layer (EDL) at the liquid/graphene interface with effective capacitance thickness ≈ 1 nm over graphene, as shown in Figure S16b schematically. The modulation speed of this graphene-EDL heterostructure is determined by both the capacitance dynamics and ion diffusion. Stabilized by the TEC (around 323K), the capacitance response limit is under 1 MHz, which is influenced by the diffusion coefficient of the DEME-TSFI 10^{-10} m^2/s [S39, S40]. Determined by the Fick's law, diffusion time of the ions equals $x^2/2D$ approximately, here D is the diffusion coefficient, x is the average distance of the ion diffusion. In the micrometer-scale heterostructure, for graphene modulation in range of 0.59 eV to 0.62 eV, diffusion time is on hundreds ns level. Moreover, to verify the GVD modulation is induced mainly by graphene rather than ionic motion, we measured the GVD influenced by the ion-gel only. The setup is shown in Figure S16c. Here a microfiber based Mach-Zehnder interferometer (MZI) is applied to check the GVD modification. The microfiber is embedded in the ion, but far away enough from the electrodes. The diameter of the microfiber is controlled as ≈ 3 μm, ensuring ≈ 8% mode field overlapping in the ion-gel, similar to our graphene based heterostructure. GVD of the MZI is optimized at ≈ -47 fs^2/mm. By checking the FSR non-equidistance [S36], we plot correlation of the gate voltage and the GVD, in Figure S16d. GVD modification induced by the ion motion is measured to be two orders-of-magnitude smaller than in the graphene-SiN heterostructure.

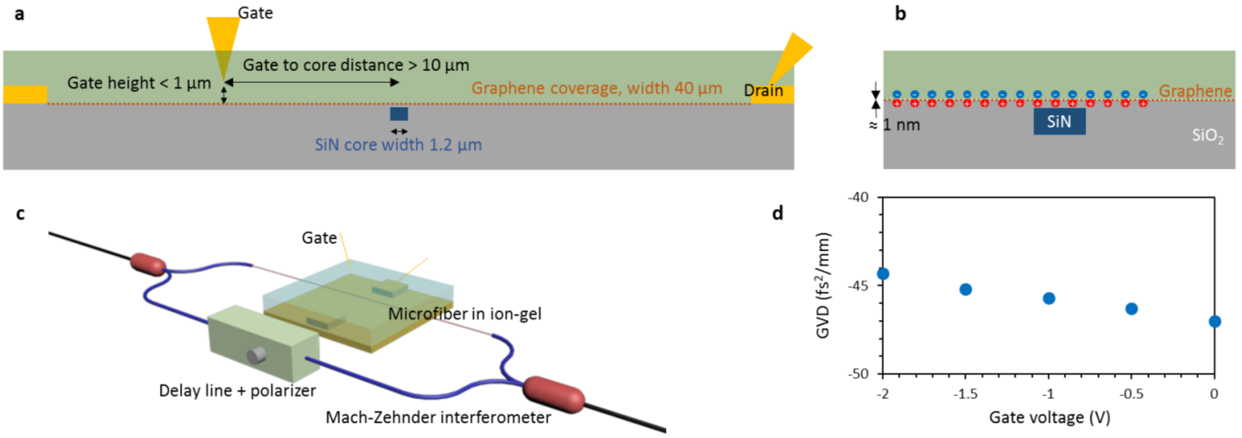

Figure S16 | Measurements of ion-gel influence on the group velocity dispersion control. a, Cross-sectional view of the heterogeneous graphene-nitride structure. **b,** Schematic diagram of the electric double layer on graphene/ion-gel interface. **c,** Mach-Zehnder setup for GVD measurement on the ion motion effects, without graphene. **d,** GVD modification induced by gating the ion-gel.

Supplementary References

S1. Mikhailov, S.& Ziegler, K. New electromagnetic mode in graphene. Phys. Rev. Lett. **99**, 016803 (2007).

S2. Hanson, G. W. Dyadic Green's functions and guided surface waves for a surface conductivity model of graphene. J. App. Phys. **103**, 064302 (2008).

S3. Vakil, A. & Engheta, N. Transformation optics using graphene, Science **332**, 1291 (2011).

S4. Lee, S. Colloidal superlattices for unnaturally high index metamaterials at broadband optical frequencies. Opt. Express **23**, 28170-28181 (2015).

S5. Yang, L. Pei, C., Shen, A., Zhao, C., Li, Y., Li, X., Yu, H., Li, Y., Jiang, X. & Yang, J. An all-optical modulation method in sub-micron scale. Sci. Rep. **5**, 9206 (2015).

S6. Yao, B, Rao, Y., Wang, Z., Wu, Y., Zhou, J., Wu, H., Fan, M., Cao, X., Zhang, W., Chen, Y., Li, Y., Churkin, D., Turitsyn, S. & Wong, C. W. Graphene based widely-tunable and singly-polarized pulse generation with random fiber lasers. Sci. Rep. **5**, 18526 (2015).

S7. Seki, S., Tsuzuki, S., Hayamizu, K., Umebayashi, Y., Serizawa, N., Takei, K. & Miyashiro, H. Comprehensive refractive index property for room-temperature ionic liquids. J. Chem. & Eng. Data **57**, 2211-2216 (2012).

S8. Sorianello, V., De Angelis, G., Cassese, T., Midrio, M., Romagnoli, M., Mohsin, M., Otto, M., Neumaier, D., Asselberghs, I., Van Campenhout, J. & Huyghebaert, C. Complex effective index in graphene-silicon waveguides. Opt. Express **24**, 29984-29993 (2016).

S9. Du, W., Li. E. & Hao, R. Tunability analysis of a graphene-embedded ring modulator. IEEE Photon. Tech. Lett. **26**, 2008 (2014).

S10. Bollinger, A., Dubuis, G., Yoon, J., Pavuna, D., Misewich, J. & Bozovic, I. Superconductor–insulator transition in $La_{2-x}Sr_xCuO_4$ at the pair quantum. Nature **472**, 458–460 (2011).

S11. Srinivasan, K. & Painter, O. Linear and nonlinear optical spectroscopy of a strongly coupled microdisk–quantum dot system. Nature **450**, 862-865 (2007).

S12. Groblacher, S. Hammerer, K., Vanner, M. R. & Aspelmeyer, M. Observation of strong coupling between a micromechanical resonator and an optical cavity field. Nature **460**, 724–727 (2009).

S13. Zhu, J., Ozdemir, S., Xiao, Y., Li, L., He, L., Chen, D. & Yang, L. On-chip single nanoparticle detection and sizing by mode splitting in an ultrahigh-*Q* microresonator. Nature Photon. **4**, 46-49 (2010).

S14. Coen, S. & Haelterman, M. Modulational instability induced by cavity boundary conditions in a normally dispersive optical fiber. Phys. Rev. Lett. **79**, 4139 (1997).

S15. Huang, S., Zhou, H., Yang, J., McMillan, J. & Matsko, A., Yu, M., Kwong, Maleki, L. & Wong, C. Mode-locked ultrashort pulse generation from on-chip normal dispersion microresonators. Phys. Rev. Lett. **114**, 053901 (2015).

S16. Coen, S., Randle, H., Sylvestre, T. & Erkintalo, M. Modeling of octave-spanning Kerr frequency combs using a generalized mean-field Lugiato–Lefever model. Opt. Lett. **38**, 37 (2013).

S17. Boyd, R. Nonlinear optics. Third Edition (Elsevier, San Diego, USA, 2003).

S18. Herr, T., Hartinger, K., Riemensberger, J., Wang, C. Y., Gavartin, E., Holzwarth, R., Gorodetsky, M. L. & Kippenberg, T. Universal formation dynamics and noise of Kerr-frequency combs in microresonators. Nature Photon. **6**, 480 (2012).

S19. Hendry, E., Hale, P., Moger, J., Savchenko, A. & Mikhailov, S. Coherent nonlinear optical response of graphene. Phy. Rev. Lett. **105**, 097401 (2010).

S20. Gu, T., Petrone, N., McMillan, J., Zande, A., Yu, M., Lo, G. Kwong, D., Hone, J. & Wong, C. Regenerative oscillation and four-wave mixing in graphene optoelectronics. Nature Photon. **6**, 554–559 (2012).

S21. Wu, Y., Yao, B., Feng, Q., Cao, X., Zhou, X., Rao, Y., Gong, Y., Zhang, W., Wang, Z., Chen, Y. & Chiang, K. Generation of cascaded four-wave-mixing with graphene-coated microfiber. Photon. Research **3**, A64 (2015).

S22. Ooi, K., Ang, L. & Tan, D. Waveguide engineering of graphene's nonlinearity. Appl. Phys. Lett. **105**, 111110 (2014).

S23. Alexander, K., Savostianova, N., Mikhailov, S., Kuyken, B. & Thourhout, D. Electrically tunable optical nonlinearities in graphene-covered SiN waveguides characterized by four-wave mixing. ACS Photonics **4**, 3039 (2017).

S24. Skryabin, D. & Gorbach, A. Colloquium: Looking at a soliton through the prism of optical supercontinuum. Rev. Mod. Phys. **82**, 1287 (2010).

S25. Erkintalo, M., Murdoch, S., Dudley, J. & Genty, G. Cascaded phase matching and nonlinear symmetry breaking in fiber frequency combs. Phys. Rev. Lett. **109**, 223904 (2012).

S26. Brasch, V., Geiselmann, M., Herr, T., Lihachev, G. Pfeiffer, M., Gorodetsky, M., & Kippenberg, T. J. Photonic chip–based optical frequency comb using soliton Cherenkov radiation. Science **351**, 357-360 (2016).

S27. Huang, S.-W., Yang, J., Yang, S.-H., Yu, M., Kwong, D.-L., Zelevinsky, T., Jarrahi, M. & Wong, C. W. Globally stable microresonator Turing pattern formation for coherent high-power THz radiation on-chip. Phys. Rev. X **7**, 041002 (2017).

S28. Coillet, A., Balakireva, I., Henriet, R., Saleh, K., Larger, L., Dudley, J. M., Menyuk, C. R. & Chembo, Y. K. Azimuthal Turing patterns, bright and dark cavity solitons in Kerr combs generated with whispering-gallery-mode resonators. IEEE Photon. **5**, 6100409 (2013).

S29. Wabnitz, S. Suppression of interactions in a phase-locked soliton optical memory. Optics Lett. **18**, 601 (1993).

S30. Herr, T., Brasch, V., Jost, J. D., Wang, C. Y., Kondratiev, N. M., Gorodetsky, M. L., & Kippenberg, T. J. Temporal solitons in optical microresonators. Nature Photonics **8**, 145 (2014).

S31. Parra-Rivas, P., Gomila, D., Matías, M. A., Coen, S. & Gelens, L. Dynamics of localized and patterned structures in the Lugiato-Lefever equation determine the stability and shape of optical frequency combs. Phys. Rev. A **89**, 043813 (2014).

S32. Huang, S., Yang, J., Yu, M., McGuyer, B. & Kwong, D. Zelevinsky, T. & Wong, C. A broadband chip-scale optical frequency synthesizer at 2.7×10^{-16} relative uncertainty. Science Adv. **2**, 1501489 (2016)..

S33. Grelu, P. & Akhmediev, N. Dissipative solitons for mode-locked lasers. Nature Photon. **6**, 84 (2012).

S34. Marin-Palomo, P., Kemal, J., Karpov, M., Kordts, A., Pfeifle, J., Pfeiffer, M., Trocha, P., Wolf, S., Brasch, V., Anderson, M., Rosenberger, R., Vijayan, K., Freude, W., Kippenberg, T. & Koos, C. Microresonator-based solitons for massively parallel coherent optical communications. Nature **546**, 274 (2017).

S35. Paccianti, M., Pasquazi, A., Park, Y., Little, B., Chu, S., Moss, D. & Morandotti, R. Demonstration of a stable ultrafast laser based on a nonlinear microcavity. Nature Comm. **3**, 765 (2012).

S36. Liu, Y., Cheng, R., Liao, L., Zhou, H., Bai, J., Liu, G., Liu, L., Huang, Y. & Duan, X. Plasmon resonance enhanced multicolour photodetection by graphene. Nature Comm. **2**, 579 (2011).

S37. Huang, S., Liu, H., Yang, J., Yu, M., Kwong, D. & Wong, C. W. Smooth and flat phase-locked Kerr frequency comb generation by higher order mode suppression. Sci. Reports **6**, 26255 (2016).

S38. Gilbert, S., Swann, W., & Wang, C. Hydrogen Cyanide H13C14N absorption reference for 1530 nm to 1565 nm wavelength calibration – SRM 2519a. Natl. Inst. Std. Technol. Spec. Publ. **260**, 137 (2005).

S39. Fujimotoa, T. & Awaga, K. Electric-double-layer field-effect transistors with ionic liquids. Phys. Chem. Chem. Phys. **15**, 8983 (2013).

S40. Sato, T., Morinaga, T., Marukane, S., Narutomi, T., Igarashi, T., Kawano, Y., Ohno, K., Fukuda, T. and Tsujii, Y. Novel solid-state polymer electrolyte of colloidal crystal decorated with ionic-liquid polymer brush. Adv. Mater. **23**, 4868 (2011).